Carbon 231 (2025) 119689

Contents lists available at ScienceDirect

Carbon

journal homepage: www.elsevier.com/locate/carbon

Investigating the formation of soot in CH_4 pyrolysis reactor: A numerical, experimental, and characterization study

Akash Bhimrao Shirsath [a], Manas Mokashi [a], Reihaneh Pashminehazar [a], Ahmet Çelik [a], Patrick Lott [a], Steffen Tischer [b], Jan-Dierk Grunwaldt [a,b], Olaf Deutschmann [a,b,*]

[a] Institute for Chemical Technology and Polymer Chemistry (ITCP), Karlsruhe Institute of Technology (KIT), 76131, Karlsruhe, Germany
[b] Institute of Catalysis Research and Technology (IKFT), Karlsruhe Institute of Technology (KIT), 76344, Eggenstein-Leopoldshafen, Germany

ARTICLE INFO

Keywords:
Methane pyrolysis
Soot formation
Carbon deposition
Chemical kinetics
Characterization

ABSTRACT

Methane pyrolysis is a promising method for eco-friendly hydrogen production, but soot formation and carbon interaction pose challenges for scaling up. Therefore, understanding the dynamics of soot formation and carbon deposition is crucial. This study delves into the intricacies of soot formation in methane pyrolysis under industrially relevant conditions, namely operations at atmospheric pressure, employing a H_2:CH_4 ratio of 2 and exploring a range of hot zone temperatures (1473 K, 1573 K, 1673 K, and 1773 K) with a 5 s residence time. Utilizing a detailed gas-phase kinetic model with direct carbon deposition reactions, the research adopts the method of moments coupled with a one-dimensional plug flow reactor model to simulate soot formation. The model is validated by characterizing soot particles that were produced in a pyrolysis reactor by means of transmission electron microscopy, Dynamic light scattering (DLS), and Raman spectroscopy. Results show that lower temperatures lead to nucleation-dominated growth, whereas higher temperatures significantly restrain particle growth due to carbon deposition. DLS data indicate a complex balance between particle growth and deposition processes. These findings provide insights into operational parameters that can enhance reactor performance and sustainability in hydrogen production processes by mitigating soot and carbon deposition.

1. Introduction

As environmental concerns become increasingly urgent, the world is turning to sustainable energy solutions to reduce the impact of traditional fossil fuels [1–3]. While these fuels have been the primary energy source for decades, they contribute heavily to carbon dioxide (CO_2) emissions, making CO_2 capture and storage crucial in combating global warming [4]. Currently, standard methods for hydrogen (H_2) production, such as steam methane (CH_4) reforming (SMR) [5,6], dry methane reforming (DMR) [7–9], auto thermal reforming of methane (ATR) [7], and catalytic partial oxidation of methane (CPOX) [10–13], emit more CO_2 and aggravate the problem [14–16]. On the other hand, CH_4 pyrolysis offers a CO_2-free alternative for H_2 production by breaking down CH_4 into "turquoise H_2" and solid carbon [17–23]. Moreover, the solid carbon can be used for various industrial applications without environmental harm [17,24–26]. Sequestration, or preferentially the use of accruing carbon for material production, significantly reduces the carbon footprint of H_2 gained by means of pyrolysis [27,28]. Renewable H_2 production technologies, such as water splitting through green electrolysis, are now gaining traction as a viable alternative to fossil fuels [29,30]. However, it is worth noting that these technologies are still under development and can be expensive to operate on a large scale [31,32]. These advancements are critical not only in addressing environmental concerns but also in shaping a carbon-neutral future.

The flow reactor system has become a prevalent choice for CH_4 pyrolysis, with research accounting for both H_2 and solid carbon production [22,23,33,34]. In addition, methane pyrolysis is performed using other reactor configurations such as packed-bed, fluidized bed, bubble column, and empty reactors [17,18,21,23,35,36,37]. However, a closer examination of CH_4 pyrolysis reveals intricate challenges, particularly concerning the formation and deposition of soot and carbon [23,38]. During the pyrolysis process, at elevated temperatures, the decomposition of CH_4 can lead to the generation of distinct carbon structures, including perfectly crystalline graphite-like deposits and non-graphitic structures [39–44]. Their formation can introduce operational complexities, such as reactor fouling, catalyst deactivation if heterogeneous

* Corresponding author. Bldg. 11.21, KIT-Campus South, Engesserstr. 20, 76131, Karlsruhe, Germany.
E-mail address: deutschmann@kit.edu (O. Deutschmann).

https://doi.org/10.1016/j.carbon.2024.119689
Received 1 July 2024; Received in revised form 30 September 2024; Accepted 5 October 2024
Available online 9 October 2024

catalysts are applied for CH_4 activation, and potential reactor blockages [23,26,45,46]. The nature, structure, and reactivity of the carbon formed can vary based on several factors, including operating conditions like CH_4 and H_2 concentration in the feed, pressure, temperature, etc. [22,43,47–49]. Given the potential implications of these factors on the efficiency and reliability of CH_4 pyrolysis, it becomes paramount to understand the underlying mechanisms of soot and carbon formation.

Several kinetic mechanisms have been proposed to describe soot and carbon deposit formation, reflecting the complexity of these processes. Traditionally, soot formation was attributed to take place via polycyclic aromatic hydrocarbons (PAHs) through the hydrogen-abstraction/acetylene-addition (HACA) mechanism [44,50,51]. This pathway involves the sequential growth of PAHs, leading to soot inception. However, recent studies [38,52–55] suggest alternative pathways, such as the clustering of hydrocarbons by radical-chain reactions (CHRCR) [52], where resonance-stabilized hydrocarbon radicals form carbon clusters. These clusters grow through low-barrier hydrogen-abstraction and hydrogen-ejection reactions, providing a more reactive and thermodynamically favorable route for soot formation [52,53,56–58]. This mechanism explains the formation of particles in conditions unsuitable for classical nucleation or simple van der Waals dimerization, addressing the limitations of older mechanisms that did not account for reactive intermediates or larger molecular structures. Moreover, studies also suggest that carbon deposition on reactor walls occurs through surface reactions [59,60] of light hydrocarbons like CH_4, C_2H_4, and C_2H_2, which decompose at high temperatures to form graphite-like carbon deposits [22,23,61–63]. Both gas-phase mechanisms (HACA and CHRCR) and surface deposition reactions highlight the diverse pathways in soot and carbon formation, necessitating comprehensive modeling and simulation to better understand these phenomena.

Soot formation during gas-phase reactions is a multifaceted process involving nucleation, coagulation, sintering, surface growth, and condensation. Over time, scientific understanding of the origins of soot has evolved. While various theories have been proposed regarding soot formation pathways, it is now widely accepted that PAHs are key intermediates in soot formation [38]. The nucleation of soot particles is a complex process with multiple potential precursors. Although older studies suggested that the pyrene ($C_{16}H_{10}$) dimer could act as a primary soot nucleating species [51,64], more recent research [52,54,65–67] indicates that $C_{16}H_{10}$ dimerization is not thermodynamically feasible at typical soot-formation temperatures and atmospheric pressure. Instead, for simplification, $C_{16}H_{10}$ is often used as a proxy for soot inception in empirical models [51,68,69]. Moreover, recent studies have highlighted the roles of both lighter and heavier PAHs [70,71], as well as resonance-stabilized radicals and radical-chain reactions [52,55], which contribute to more reactive clustering mechanisms under these conditions. Following the particle inception phase, soot formation progresses through several stages, including coagulation, surface growth, and aggregation. The process begins with the transition from gas-phase soot precursors to liquid-like incipient particles, which then grow rapidly through both coagulation and gas-to-particle conversion [72]. Coagulation involves smaller particles colliding and sticking together to form larger particles, a process particularly prominent at higher temperatures where increased thermal energy enhances particle collision frequency [73–75]. During this stage, particles may undergo coalescence, merging into a single larger particle, or form aggregates that maintain their individual particle boundaries but are held together by van der Waals forces or chemical bonds. The shape and size of these aggregates significantly influence their coagulation dynamics and growth rates [73,76,77]. Surface growth follows, involving the adsorption and reaction of gas-phase species, such as acetylene, on particle surfaces, which leads to further soot particle growth. This stage is often governed by mechanisms such as HACA [44,50,51] and CHRCR [52].

To simulate and understand the complexities of soot particle formation and growth, various modeling approaches have been developed. These include the monodisperse model [78–80], the method of moment [44,81,82], the sectional method [34,83], the stochastic model [84], and the Galerkin model [85]. Among others, Frenklach et al. [50,51,86] used the method of moments and applied detailed chemical kinetics to study the formation and growth of soot particles via PAHs. Researchers have also employed various modeling approaches, including 1D, 2D, and 3D models, to simulate soot formation and growth in flow reactors [69,87–92]. One-dimensional (1D) plug flow reactor models are commonly employed due to their simplicity and reduced computational cost, but they often fail to capture the full scope of real-world reactor conditions, where significant radial gradients in temperature, species concentration, and particle sizes exist [69,92]. Recent studies [69,91] have implemented two-dimensional (2D) models that incorporate radial effects, providing a more accurate representation of soot and nanoparticle formation dynamics within laminar flow reactors. Additionally, three-dimensional (3D) computational fluid dynamics (CFD) models offer a comprehensive analysis by capturing interactions between flow fields, chemical reactions, and particle dynamics, improving soot formation predictions under diverse conditions [89,93]. Despite significant advancements in understanding the kinetics of soot formation during CH_4 pyrolysis, primarily through PAHs, there remains a gap in the comprehensive study of combined kinetics. Specifically, the interplay between soot formation via PAHs and direct carbon deposition reactions on reactor wall driven by light hydrocarbons has yet to be thoroughly explored.

This paper presents a comprehensive study of soot formation considering carbon deposition reaction in a CH_4 pyrolysis in an empty reactor using the method of moments, which comprises simultaneous chemical reactions, coagulation, and surface growth (see Fig. 1). A one-dimensional plug flow reactor (PFR) model was combined with the method of moments for a more holistic simulation of CH_4 pyrolysis. This integrated model incorporates the detailed gas-phase chemical kinetics of Appel, Bockhorn, and Frenklach (ABF) [51], along with direct surface deposition reactions of light hydrocarbons. Additionally, CH_4 pyrolysis experiments in the tubular reactor (without catalyst) under industrially relevant conditions were conducted to validate the model, and characterization techniques, including transmission electron microscopy (TEM), dynamic light scattering (DLS), and Raman spectroscopy, were employed to analyze the collected soot samples. Through this multifaceted approach, the study deepens the understanding of the intricate processes governing simultaneous carbon deposits on reactor wall and soot formation and paves the way for optimizing CH_4 pyrolysis reactors for cleaner and more efficient H_2 and carbon production.

2. Experimental methodology

2.1. Experiment

CH_4 pyrolysis experiments were conducted using a high-temperature-pressure reactor designed for kinetic measurements at temperatures up to 2073 K and pressures up to 10 bar and described in detail in previous publications [22,23,94]. The gas supply of the setup is realized by means of mass flow controllers (Bronkhorst). The reaction takes place in an α-Al_2O_3 tubular plug flow reactor of 1 m length and 0.2 m inner diameter within a stainless-steel vessel, heated electrically to create a 0.4 m hot zone spanning from 0.35 m to 0.75 m, and the experiments were conducted with a residence time of 5 s in the hot zone. The effluent gas was analyzed using an HPR-20 mass spectrometer (Hiden Analytical), and soot was collected at the reactor bottom for further analysis. A 2:1 molar ratio of H_2:CH_4 was used as the inlet reaction gas mixture and the content of H_2, CH_4, C_2H_2, C_2H_4, C_2H_6, and C_6H_6 was analyzed in the outlet gas stream. The addition of H_2 in the feed enabled steady-state operation by reducing the rate of solid carbon formation on reactor wall, allowing for reactor operation over extended periods. The experiments were performed under atmospheric pressure, with hot zone temperature varied at 1473 K, 1573 K, 1673 K, and 1773 K.

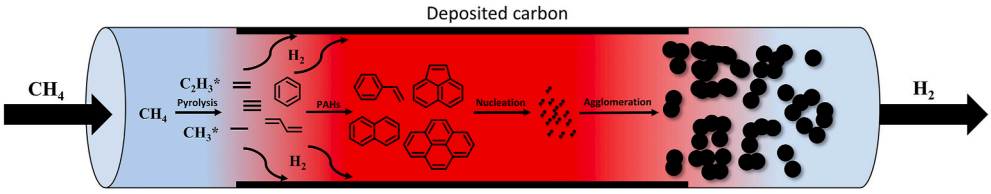

Fig. 1. Schematic overview of the soot formation and carbon deposition on reactor wall in empty tube CH4 pyrolysis reactor. (A colour version of this figure can be viewed online.)

2.2. Characterization

In order to comprehensively understand the properties of the soot samples collected at the bottom of the reactor, Raman spectroscopy, TEM, and DLS analysis were applied. Raman spectroscopy, which is sensitive to both crystal and molecular structures, was used to determine the different carbon allotropes and disordered varieties present in the samples [95–97]. TEM was used to investigate the aggregate shape and the size of primary particles by providing high-resolution images of the soot samples. DLS analysis was performed to measure the hydrodynamic diameter of particles by analyzing their Brownian motion and correlating it to their size. More detailed information on the characterization is provided in Ref. [22]. The characterization results were used to improve and validate the soot formation model by comparing the model predictions with the experimental results, hereby providing a better understanding of the soot formation process in the CH_4 pyrolysis reactor.

3. Modeling approach and numerical simulation

3.1. Chemical kinetics

The Appel et al. [51] (ABF) reaction mechanism is used to simulate CH_4 pyrolysis. The original mechanism comprises 544 reactions and 101 species in the gas-phase. After adaption for CH_4 pyrolysis, i.e. by removing all the oxygen-containing reactions, the modified version contains 247 reactions and 76 species [98]. It primarily focuses on C1 and C2 hydrocarbons, incorporating carbon-carbon coupling reactions to form linear hydrocarbons and benzene (C_6H_6). In ABF mechanism, the pathway for $C_{16}H_{10}$ formation involves several steps, beginning with the formation of C_6H_6 through propargyl radical, C_4H_x, and C_6H_x pathways that include cyclization reactions. The growth of PAHs up to $C_{16}H_{10}$ occurs via HACA mechanism, progressing through intermediates such as naphthalene and phenanthrene. Sequential additions of C_2H_2 or C_4H_4 facilitate aromatic ring growth, with key radicals like phenyl, benzyne, phenylacetylene, and biphenyl playing crucial roles in this process, ultimately leading to pyrene formation (see Ref. [98] for more details). As mentioned earlier, recent studies [65,99–102] suggest that, in addition to HACA, mechanisms like CHRCR [52] are also significant in the growth of PAHs, including $C_{16}H_{10}$. The CHRCR mechanism involves the formation of larger hydrocarbon clusters from smaller radicals through low-barrier hydrogen-abstraction and hydrogen-ejection reactions, providing a more reactive route for soot inception and growth. In addition to ABF, with recent advancements in the field of soot modeling, more detailed mechanisms like Pejpichestakul et al. (CRECK) [103] and Blanquart et al. (Caltech) [104] could be explored in future studies. However, the ABF mechanism offers a computational advantage over these more complex mechanisms, making it attractive for scale-up studies. Although pyrene dimerization is not thermodynamically favorable and does not lead to nucleation under typical soot-formation conditions, the present study uses it as an empirical proxy to represent the physical mechanism of soot inception. In the current model, the chemical source term used is the net production rate of the $C_{16}H_{10}$ dimers as a proxy for soot inception. The nucleation rate is assumed to be the collision rate of two A4 ($C_{16}H_{10}$) molecules in the free-molecular region, with a van der Waals enhancement factor of 2.2 considered [44,105–107]. More information on the kinetics is provided in Refs. [22,98].

Soot surface growth in CH_4 pyrolysis is governed by several key mechanisms, including HACA [51,86], PAHs adsorption [86,108–110], and CHRCR [38,52–55]. The HACA mechanism, developed by Frenklach et al. [51,86], proposes that soot particles grow through the addition of carbon atoms to their surfaces via hydrogen abstraction from gas-phase precursor molecules, followed by acetylene addition. In addition to the HACA mechanism, the adsorption of larger hydrocarbons, particularly PAHs, onto soot surfaces contributes significantly to soot growth. PAH adsorption involves the collision and adherence of PAH molecules onto soot particles, enhancing mass growth, especially under conditions favorable for the condensation of larger aromatic species. For our present study, the HACA surface growth mechanism was modified by eliminating the oxygen-related reactions (summarized in Table S1). It should be noted that this study assumes soot surface growth occurs primarily on primary particles rather than on aggregates [86]. Additionally, the fraction of surface site (α) parameter (Equation S1) was tuned to 0.2 to achieve a better fit with the experimental results, particularly when considering the effects of direct carbon deposition reactions.

As mentioned in the introduction, direct carbon deposition on the reactor wall is a significant factor, alongside soot formation, during CH_4 pyrolysis. This deposition is caused by surface reactions involving light hydrocarbons from gas-phase, namely CH_4, C_2H_2, C_2H_4, C_2H_6, C_4H_6 and C_6H_6 [35,62,63]. These small hydrocarbons are assumed to deposit on the reactor wall surfaces due to their high reactivity and abundance under pyrolysis conditions [59,20,111,112]. Unlike larger PAHs, which are generally associated with the inception of soot particles, the deposition on reactor walls is primarily driven by smaller hydrocarbons that can readily undergo surface reactions, particularly on the hot surfaces of the reactor. The deposition mechanism involves the adsorption of these small hydrocarbons onto the reactor walls, followed by surface reactions such as HACA mechanism, which integrate them into the growing carbon structure [59,61,62,63,111,43,112,113]. This process is effective because smaller hydrocarbons can easily chemisorb and react on the surface, leading to the formation of solid carbon, while the role of PAHs in direct surface deposition remains minimal [59,111,20]. These surface reactions are also prone to H_2 inhibition [114]. The reaction mechanism was initially proposed by Becker et al. [115] and later refined by Li and Deutschmann [63]. The kinetic mechanism employed for this study can be found in Table S2. More detailed information on the kinetic mechanism of carbon deposition on reactor wall is provided in Ref. [35].

3.2. Plug flow reactor

The CH_4 pyrolysis experiments in the tubular reactor were simulated using a one-dimension PFR model, which was implemented as FORTRAN code and coupled with the DETCHEM software package [22,116,117]. The model simulates the chemically reacting flow of a gas mixture under steady-state conditions, and it solves continuity equations, species conservation equations, and equations of state using a differential-algebraic solver (LIMEX) [118]. The model assumes no changes in radial properties and plug flow behavior, which is supported

by the Peclet number for heat and mass ($Pe^{*}\frac{R}{z} > 1$) values used in this study [69,117,119,120].

The model allows for axial changes in gas properties while assuming no change in radial properties.

The equation of continuity, represented by Equation (1), is used to calculate mass flux in a system.

$$\frac{d(\rho u)}{dz} = P' \sum_{i \in S_g} M_i \dot{s}_i \tag{1}$$

Where, ρ is the gas-phase density, M_i is the molar mass of species i, z is the axial coordinate, S_g is the set of gas-phase species, $\dot{s}_i$ is the surface reaction rate at the reactor wall for species i, u is the flow velocity, and P' is the chemically active perimeter per unit length. Herein, $\dot{s}_i$ is the molar production rate of species i by the surface reaction (carbon deposition reactions) at the reactor wall is given by (2).

$$\dot{s}_i = \sum_{k \in R_s} \nu_{ik} k_k \prod_{j \in S_g \cup S_s} c_j^{\nu'_{jk}} \tag{2}$$

Herein, R_s represents the set of the reactor involving reactor wall surface carbon deposition, and S_s denotes the sets of surface species. The stoichiometric coefficients are represented by ν_{ik}, while ν'_{jk} indicates the reaction orders (equal to the stoichiometic coefficient of the reactants). The concentration of species i is denoted by c_i given as mol m^{-2} for deposited surface species and mol m^{-3} for gas-phase species. Additionally, k_k represent the rate constant of reaction k. Along with Equation (1), the species conservation Equation (3) is solved.

$$\rho u \frac{dY_i}{dz} + Y_i P' \sum_{i \in S_g} M_i \dot{s}_i = M_i (P' \dot{s}_i + \dot{\omega}_i) \tag{3}$$

where, Y_i is the mass fraction. The rate of gas-phase reaction ($\dot{\omega}_i$) of the species i is calculated as shown in (4).

$$\dot{\omega}_i = \sum_{k \in R_g} \left(\nu''_{ik} - \nu'_{ik}\right)_{k_k} \prod_{j \in S_g} c_j^{\nu'_{jk}} \tag{4}$$

where, ν'_{ik} and ν''_{ik} are the stoichiometric coefficients of the forward and reverse reactions. Furthermore, for present study, the energy balance equation is not solved. Instead, the experimentally measured temperature profile within the reactor is used as input.

3.3. Method of moments

The technical optimization of the CH_4 pyrolysis process critically depends on effectively modeling the overall process to control soot formation. Focusing on soot suppression in the gas phase is crucial as it ensures the high purity of the resulting H_2 by reducing particulate contamination, while promoting carbon deposition on the reactor walls allows for controlled carbon formation that is easier to manage. The method of moments (MOM) is a prominent model that tracks the dynamics of soot particle size and number density [38,44,74,75,121–125]. These equations are derived from the kinetic theory of gases, and take into account the effects of nucleation, growth, and coagulation of soot particles. In the context of CH_4 pyrolysis, the MOM model provides insights into soot formation mechanisms and process optimization by considering variables such as temperature, pressure, and reactant concentration.

Instead of solving for the entire particle size distribution (PSD), the present study focuses on solving the first three moments (M_0, M_1, and M_2) that capture the most important aspects of the process (see SI, Equations (S2)-(S4)). Here, M_0 represents the total number concentration, M_1 represents the total volume concentration, and M_2 represents the total surface area concentration of the soot particles. The governing equations for the log-normal moment model were written in a dimensionless form in terms of moment change rates. The zeroth moment (M_0) represents the total particle number concentration (N') and is affected by nucleation and coagulation and its rate of change shown in Equation (5).

$$\frac{dN'}{d\Theta} = I' - \xi N'^2 \tag{5}$$

where N' is the dimensionless particle number concentration, which is the ratio of M_0 (total particle number concentration) to the soot monomer concentration (n_m). The variable Θ represents the dimensionless residence time, which is a ratio of the residence time (t) to a characteristic time for particle growth (τ). For the present MOM model, the τ for particle growth is defined via Equation (6).

$$\tau = \left(n_m a_m \sqrt{\frac{k_B T}{2\pi m_m}} \right)^{-1} \tag{6}$$

Herein, a_m and m_m are the surface area and mass of the soot monomer. The I' term in Equation (5) represents the dimensionless nucleation rate. It is calculated as shown in Equation (7), where the soot nucleation rate (I_{nucl}) is derived from the net production rate of pyrene dimer (a proxy for soot inception).

$$I' = \frac{I_{nucl}}{(n_m / \tau)} \tag{7}$$

Furthermore, ξ (second term in Equation (5)) stands for dimensionless coagulation coefficient. Primarily, for conditions applied in this study, the $Kn = \lambda / d_p$ is in the range of 10–40 which corresponds to the transition regime, where λ is mean free path and d_p is characteristic length scale of the particle [126,127]. Therefore, coagulation coefficients are calculated as the harmonic average of coefficients in the free molecular (ξ_{FM}) and continuum regimes (ξ_C) (see SI, Equations (S5)-(S9)). The model can dynamically determine the appropriate regime based on the calculated Kn: $Kn < 1$ corresponds to the continuum regime, $Kn > 50$ corresponds to the free molecular regime, and $1 < Kn < 50$ indicates the transitional regime.

The first moment (M_1) represents the particle volume concentration (V'_1) and is affected by nucleation and surface growth, and its rate of change is shown in Equation (8).

$$\frac{dV'_1}{d\Theta} = I' + W' \tag{8}$$

where V'_1 is the ratio of M_1 to n_{sat} times v_m (volume of soot monomer) and W' is dimensionless soot surface growth rate. The second moment (M_2) represents the total particle surface area concentration (V'_2) and is affected by nucleation, surface growth, and coagulation, as shown in Equation (9).

$$\frac{dV'_2}{d\Theta} = I' + 2\zeta V'^2_1 + W' \tag{9}$$

where ζ is the dimensionless coagulation coefficient and is calculated as the harmonic average of coefficients in the free molecular (ζ_{FM}) and continuum regimes (ζ_C) (see SI, Equations (S10)-(S13)). Assuming spherical particles, the mean particle diameter ($d_{p,soot}$) can be calculated based on M_0, M_1 and ρ_{soot} (density of the soot particles) using Equation (10).

$$d_{p,soot} = \left(\frac{6 m_m M_1}{\pi \rho_{soot} N_A M_0} \right) \tag{10}$$

The PSD is assumed to follow a log-normal distribution, which allows the geometric mean volume (v_g, Equation (11)) and geometric standard deviation (σ_g, Equation (12)) to be expressed in terms of the first three moments (M_0, M_1 and M_2) of the PSD.

$$\nu_g = \frac{M_1^2}{M_0^{3/2} M_2^{1/2}} \tag{11}$$

and,

$$\ln^2 \sigma_g = \frac{1}{9} \ln\left(\frac{M_0 M_2}{M_1^2}\right) \tag{12}$$

4. Results and discussion

4.1. Gas-phase species profile

The experiments were conducted in the above-mentioned high-temperature setup under atmospheric conditions using a H_2:CH_4 feed gas ratio of 2 with a residence time of 5 s in the hot zone. Hot zone temperatures of 1473 K, 1573 K, 1673 K, and 1773 K were set, resulting in temperature profiles shown in Fig. 2.

Fig. 3 illustrates the experimentally measured and numerically simulated mole fraction of gas-phase species (H_2, CH_4, C_2H_2, C_2H_4, C_2H_6, and C_6H_6) as a function of hot zone temperature. It is important to note that the mole fractions of experimentally measured major gas-phase species are subject to error due to measurement uncertainties [49]. The simulations were conducted using a 1D plug flow reactor model with detailed chemical kinetics (ABF), with or without consideration of direct carbon deposition reactions. The CH_4 pyrolysis experiments demonstrate the impact of temperature on CH_4 conversion and product formation. The comparison between two scenarios highlights the significant role that direct wall-carbon deposition reactions from light hydrocarbons [35,59–61] play in CH_4 conversion: Especially as the hot zone temperature increases, the simulations that neglect wall-carbon deposition deviate from the experimental data. This deviation is due to the increasing relevance of heterogeneous reaction pathway [35], specifically direct wall-carbon deposition reactions (Table S2). Additionally, there is the potential contribution of the CHRCR (Clustering of Hydrocarbons by Radical-Chain Reactions) mechanism [52], which involves radical-chain reactions of hydrocarbons like C_2H_4 and C_2H_2 and offers another plausible pathway for carbon formation [52,53]. Both mechanisms emphasize the significant influence of light hydrocarbons in CH_4 pyrolysis, underscoring the need for further investigation into their precise roles. The experimental result (Fig. 3(a)) shows that H_2 yield correlates closely with CH_4 conversion. As the temperature rose from 1473 K to 1773 K, CH_4 conversion increased significantly from 56 % (1.21 mol-%) to 96 % (0.11 mol-%), hereby underscoring that elevated temperatures favor the endothermic pyrolysis reaction. Similarly, the yield of H_2, the primary gas-phase product, increased from 54 % (87.11 mol-%) at 1473 K to 95 % (98.63 mol-%) at 1773 K. The simulations (without carbon deposition reactions) predict an initial increase in H_2 production (84 mol-%) only up to 1573 K, followed by a decrease in H_2 mole fractions (80 mol-% at 1773 K) (Fig. 3(a)). This decrease is primarily caused by reversible reactions of light hydrocarbons taking place in the post-hot zone of the reactor, where the negative temperature gradient (~1000 K) triggers reverse gas-phase reactions (hydrogenation) of hydrocarbons like C_2H_2, that consume H_2 and forms CH_4 [98]. In contrast, the numerical prediction matches well with the experimental data for major species (H_2 and CH_4) once the deposition reactions are incorporated into the model (Fig. 3(a)). Intriguingly, no clear trend is observed for minor gas-phase species (Fig. 3(b) and (c)). At 1473 K, Fig. 3(b), C_2H_2 was found to be 0.2 mol-%, which then decreased to an almost negligible value at 1573 K, before increasing again to 0.1 mol-% at 1673 K and 0.15 mol-% at 1773 K. Furthermore, C_2H_4 with a 0.6 mol-% peaks at 1673 K, but decreases substantially by 1773 K, indicating further decomposition at higher temperatures. In contrast, Fig. 3(c), C_2H_6 remains present across all temperatures but decreases as the temperature rises. Except at 1473 K, C_6H_6 is found only in trace amounts. Additionally, it is important to note that the concentrations of these gaseous by-products are close to the calibration limits of the analytical instruments, with an estimated measurement error of up to ±5 %, limiting the precision to general trends [49].

Overall, simulations that include carbon deposition reactions from light hydrocarbons on the reactor wall show better agreement with the experimental results. The significant influence of light hydrocarbon species in CH_4 pyrolysis is highlighted, suggesting the necessity for further investigation into their specific roles and interactions to refine the understanding of carbon formation pathways.

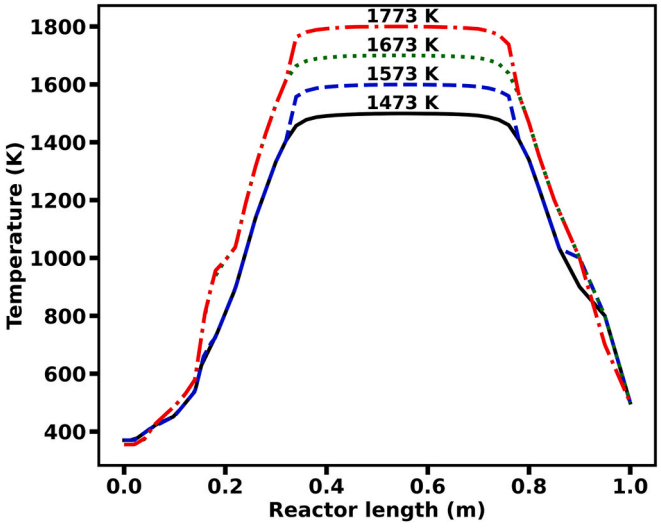

Fig. 2. Experimentally measured temperature at inlet gas feed composition of H_2:CH_4 = 2:1 and hot zone temperature of 1473 K, 1573 K, 1673 K, and 1773 K. (A colour version of this figure can be viewed online.)

4.2. Spatially-resolved species profile

Fig. 4 depicts the numerically simulated axially resolved gas-phase species profiles within the CH_4 pyrolysis reactor. The full reactor simulations were performed at hot zone temperatures ranging from 1473 K to 1773 K (including preheat and post-hot zone, c. f. Fig. 2), either without or with incorporation of carbon deposition reactions (Table S2).

Numerically simulated, Fig. 4(a)–(d), profiles of H_2 and CH_4 mole fractions change immediately once the feed gas enters the hot zone entrance of the reactor: CH_4 is decomposed, which results in H_2 formation, with increased H_2 production at higher temperatures. Notably, simulations without carbon deposition show a post-hot zone decline in CH_4 conversion, which can be attributed to reversible reactions, specifically the hydrogenation reaction of gas-phase species like C_2H_2, C_2H_4, and C_2H_6, at temperatures around 1000 K [98]. In contrast, simulations that take carbon deposition into account predict only minor decreases in CH_4 conversion, which suggest the competitive rate between direct deposition and reversible gas-phase reactions in post-hot zone of the reactor.

Fig. 4(e)–(h) focuses on the minor gas-phase species C_2H_2 and C_2H_4. The simulations are consistent with previous studies [21,23,98,128] and emphasize the critical role of C_2H_2 as an intermediate. In both scenarios (with or without carbon deposition reactions), C_2H_2 concentrations peak within 1–3 mm of the hot zone with up to 11 mol-% within hot zone of the reactor before declining due to forward reactions that lead to PAHs formation and soot surface growth. The decline is more pronounced in simulations that take carbon deposition reactions into account, particularly underscoring its increased consumption at higher temperatures. Conversely, C_2H_4, the second most significant by-product after C_2H_2, is formed in smaller quantities. However, its formation is delayed with respect to position in the reactor due to its involvement in carbon deposition reactions. Furthermore, under both conditions, it can be observed that as the temperature increases the formation C_2H_4 shifts

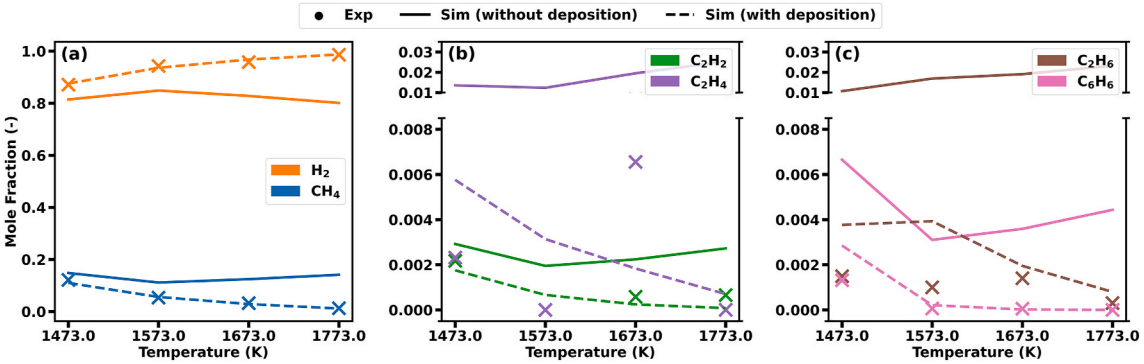

Fig. 3. Comparison of experimentally measured end-of-pipe and numerical results obtained either under consideration of wall-carbon deposition (dashed line) or without direct carbon deposition reactions (solid line) of (a) H_2 and CH_4, (b) C_2H_2 and C_2H_4 and (c) C_2H_6 and C_6H_6 gas-phase species as a function of temperatures; inlet gas feed composition of H_2:CH_4 = 2:1 and residence time of 5 s. (A colour version of this figure can be viewed online.)

close to the entrance of the hot zone of the reactor. In the hot zone of the reactor, C_2H_4 is formed and subsequently consumed to form C_2H_2 species via the C_2H_3 intermediate. However, simulations incorporating direct carbon deposition reactions indicate a higher consumption rate of C_2H_4, as it also contributes to the formation of solid carbon. In the post-hot zone of the reactor, there is a transient increase and subsequent decrease in C_2H_4 as it is consumed to reform CH_4. The C_2 species (C_2H_4 and C_2H_2) are partly consumed via reversible reactions to form intermediates, C_2H_3, C_2H_6, and CH_3 radical, which lead to CH_4 formation [98].

Lastly, Fig. 4(i)–(l) presents the mole fractions of C_6H_6 and $C_{16}H_{10}$. The simulation results show that the absolute peak mole fractions of $C_{16}H_{10}$ formed is comparatively lower by orders of magnitude compared to other light hydrocarbons and C_6H_6. It should be noted that, due to experimental limitations, the concentration of $C_{16}H_{10}$ could not be measured. Nevertheless, they are of high relevance as soot precursors. As the gas feed enters the hot zone of the reactor, C_6H_6 is produced via the C_3H_3 recombination reaction among others [98]. Within the hot zone of the reactor, C_6H_6 is consumed to form the PAHs (up to $C_{16}H_{10}$), and its consumption increases with an increase in temperature. Following this, C_6H_6 reformation is observed in the post-hot zone. In addition to the C_2 and C_4 species, the formation of C_6H_6 can be attributed to reversible breakdown of larger hydrocarbons or PAHs in post-hot zone, driven by negative temperature gradients [98]. In contrast, the simulation performed taking carbon deposition reactions, C_6H_6 consumed at even higher rate via direct carbon deposition reaction (Table S2) which also increases with increasing in temperature. Analogous to simulation without direct carbon deposition reaction, C_6H_6 formation take place in the post-hot zone of the reactor; however, it is three order of magnitude lower. Furthermore, the mole fraction of $C_{16}H_{10}$ (Fig. 4(i)–(l)), which acts as a primary soot precursor (a proxy for soot inception), increases in the hot zone at first, but then diminishes due to the formation of $C_{16}H_{10}$ dimers and subsequent soot growth. Notably, Fig. S1 shows that with an increase in temperature, the formation of gas-phase $C_{16}H_{10}$ initiates earlier and becomes more pronounced. It can also be observed that the amount of $C_{16}H_{10}$ formed within the hot zone is higher in simulations excluding carbon deposition. This can be attributed to the availability of precursors (CH_4, C_2H_6, C_2H_4, C_2H_2, C_4H_6, and C_6H_6) that are otherwise consumed during carbon deposition. Followed to this, the mole fraction of $C_{16}H_{10}$ begins to decrease as soot precursors start to form. Furthermore, in the post-hot zone of the reactor, reversible reactions induced by negative temperature gradients lead to the breakdown of $C_{16}H_{10}$ smaller PAHs and C_6H_6 (Fig. 4(i)–(l)). The significant increase of $C_{16}H_{10}$ at higher temperatures indicates the complex reaction networks, HACA, that contribute to soot precursor formation. Alternatively, the CHRCR mechanism [52] offers another pathway for carbon growth. In this mechanism, hydrocarbons like C_2H_4 participate in radical-chain reactions involving resonance-stabilized radicals, such as C_2H_4 and C_2H_2, leading to the formation of solid carbon clusters. This indicates that under certain conditions, hydrocarbons like C_2H_4 do not merely decompose but contribute to the growth of solid carbon through radical-chain reactions. Further study is needed to determine which mechanism predominates under the specific conditions of CH_4 pyrolysis. While this study shows that incorporating carbon deposition reactions improves agreement with experimental data, further research is essential to clarify the dominant mechanisms under different CH_4 pyrolysis conditions.

4.3. Effect of wall-carbon deposition reactions on soot formation

Expanding upon the knowledge gained from the behavior of gas-phase species, attention shifts to the intricate processes involved in soot formation. While PAHs have traditionally been considered critical intermediates in soot formation [50,51,124], recent studies suggest that closed-shell PAH species may not be the primary drivers. Instead, resonance-stabilized radicals (RSRs) and radical-chain reactions, such as CHRCR, are increasingly recognized as playing crucial roles in carbonaceous particle growth [38,56–58,129–132]. These radicals are involved in reactive clustering mechanisms (CHRCR), where they react with other hydrocarbons to form covalently bound clusters. These clusters undergo further growth through low-barrier hydrogen-abstraction and hydrogen-ejection reactions [52,54], contributing significantly to soot formation. Despite this, considering pyrene as a proxy for soot inception still provides a good approximate estimation of the onset of soot formation, as it captures the transition from gas-phase chemistry to the formation of nascent soot particles under typical combustion conditions [55,133]. For the present study the method of moments is utilized to analyze the formation and aggregation of soot, employing ABF chemical kinetics with $C_{16}H_{10}$ dimers as a proxy for soot inception. As discussed above, the direct carbon deposition reactions play a significant role during CH_4 pyrolysis, making it crucial to investigate their impact on the soot formation process.

Fig. 5 demonstrates the effect of wall-carbon deposition reactions on soot nucleation rates at various hot zone temperatures. Furthermore, the arrow between two curves shows the percentage change calculated based on the area under the curve method. In both scenarios, with and without carbon deposition reactions, an increase in temperature within the hot zone leads to an increase in soot nucleation rates (Fig. 5). Initially, there is a sharp rise in soot nucleation rate as the gas enters the hot zone, which then declines due to the reduced availability of $C_{16}H_{10}$ (Fig. 4(i)–(l)). The numerical results accounting for carbon deposition reactions show a substantially lower nucleation rate when compared to the scenario without deposition, irrespective of the reactor temperature. This suggests that the formation of $C_{16}H_{10}$ is hindered as the precursor species, specifically C_2 and C_4 hydrocarbons, are consumed in direct carbon deposition reactions, as shown in Fig. 4. Additionally, the rate of

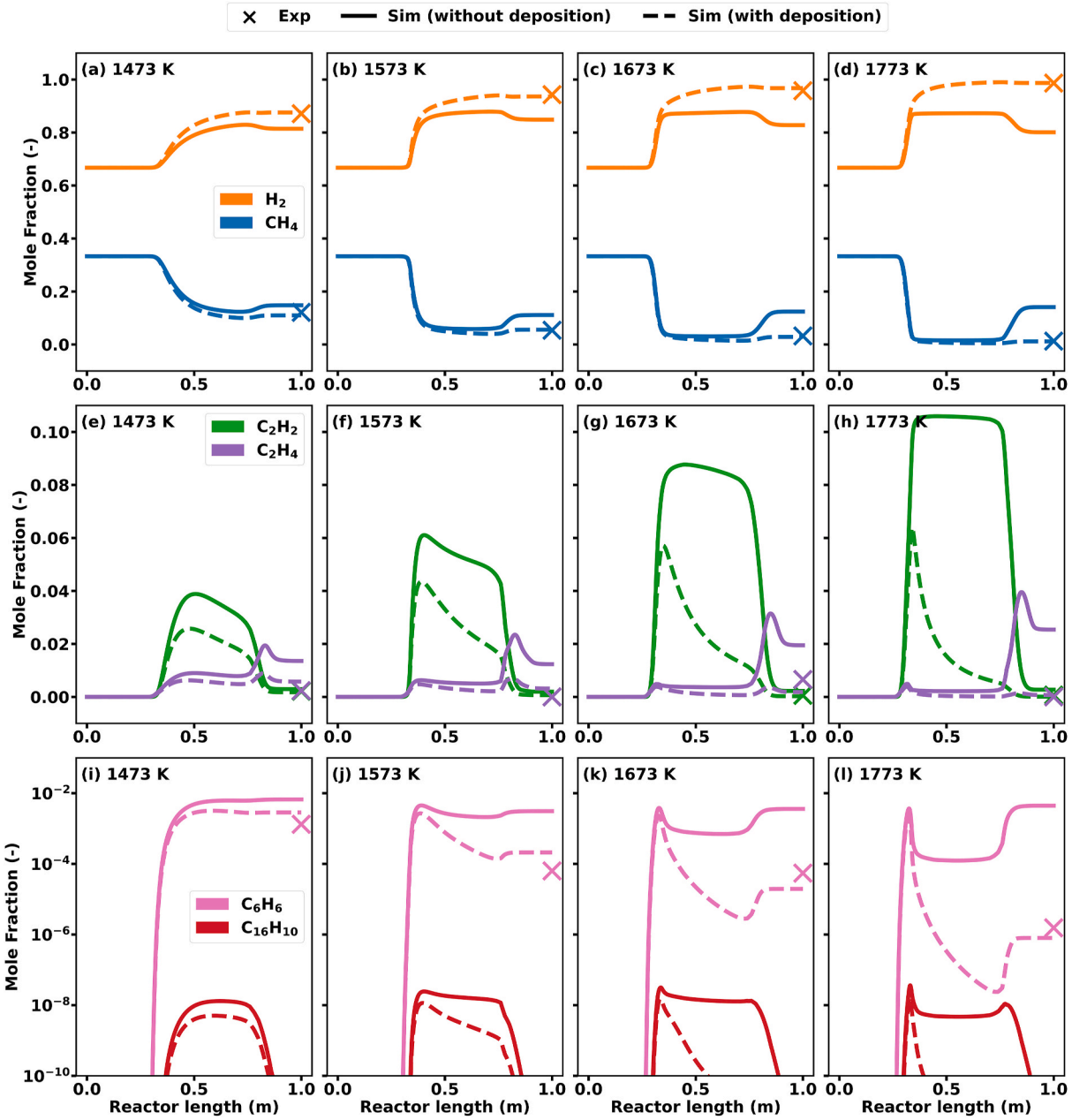

Fig. 4. Numerically predicted axially resolved profiles of gas-phase species mole fractions (with and without carbon deposition reactions) at different hot zone temperatures as well as experimental end-of-pipe data. Panels (a)–(d) display the profiles for H_2 and CH_4, panels (e)–(h) for C_2H_2 and C_2H_4, and panels (i)–(l) for C_6H_6 and $C_{16}H_{10}$, each set corresponding to the reactor temperatures of 1473 K, 1573 K, 1673 K, and 1773 K, respectively. (A colour version of this figure can be viewed online.)

carbon deposition reactions intensifies with increasing temperature, resulting in a further decrease in the nucleation rate of soot. Furthermore, in the post-hot zone of the reactor, the simulation taking carbon deposition reactions into account indicates that the reversible reactions have no considerable effect on the soot nucleation rate, as evidenced by an increased nucleation rate in the post-hot zone (Fig. 5(c) and (d)) when compared with the simulation without carbon deposition reactions. Overall, incorporating direct carbon deposition reaction leads to an approximately 90 % decrease in nucleation rate. This considerable reduction underscores the importance of including carbon deposition reactions in studies of soot formation in CH_4 pyrolysis systems.

Examining the rates of soot nucleation with and without carbon deposition reactions lays the foundation for exploring the initial and subsequent phases of soot evolution, specifically the concentration of particle numbers and the rate of coagulation, which are key information for predicting the formation and growth of soot particles. It is observed that, upon entry into the hot zone, the particle concentration increases sharply, indicating robust nucleation influenced by increased thermal conditions, as shown in Fig. 6(a)–(d). After reaching its peak, the aggregate particle number concentration begins to decrease, signaling a transition from nucleation to coagulation. Furthermore, the peak particle concentration shifts closer to the hot zone entrance with an increase in hot zone temperatures, as shown in Fig. 6(b)–(d). This shift is attributed to an acceleration of nucleation kinetics (dimer formation, Fig. 5), influenced by harsher thermal conditions.

Fig. 6 demonstrates that initially, both particle (aggregate) concentration and coagulation rates increase as the gas enters the hot zone. However, the total aggregate particle number concentration (after

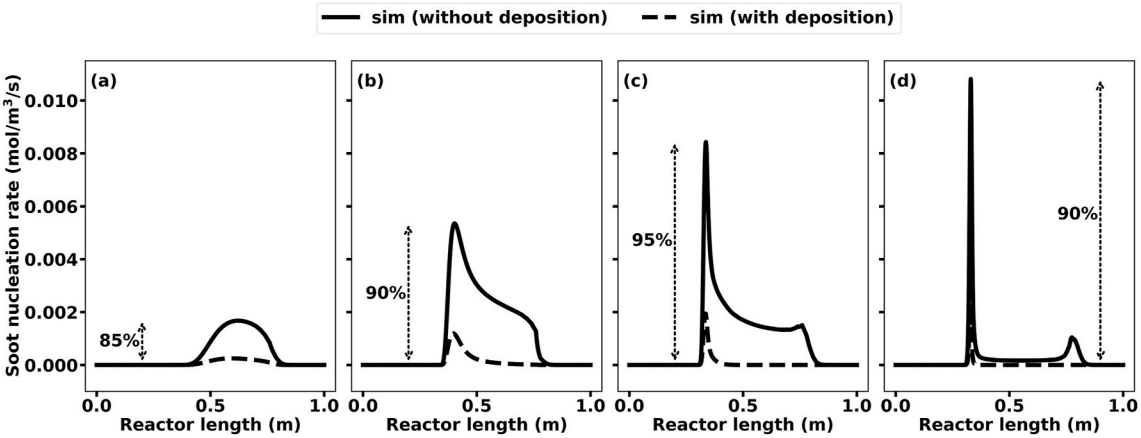

Fig. 5. Effect of direct carbon deposition reactions (reactor wall) on axially resolved soot nucleation profile (net production rate of $C_{16}H_{10}$ dimer) at hot zone temperature of (a) 1473 K, (b) 1573 K, (c) 1673 K, and (d) 1773 K. Vertical arrow shows percentage change in soot nucleation rate calculated based on area under the curve. (A colour version of this figure can be viewed online.)

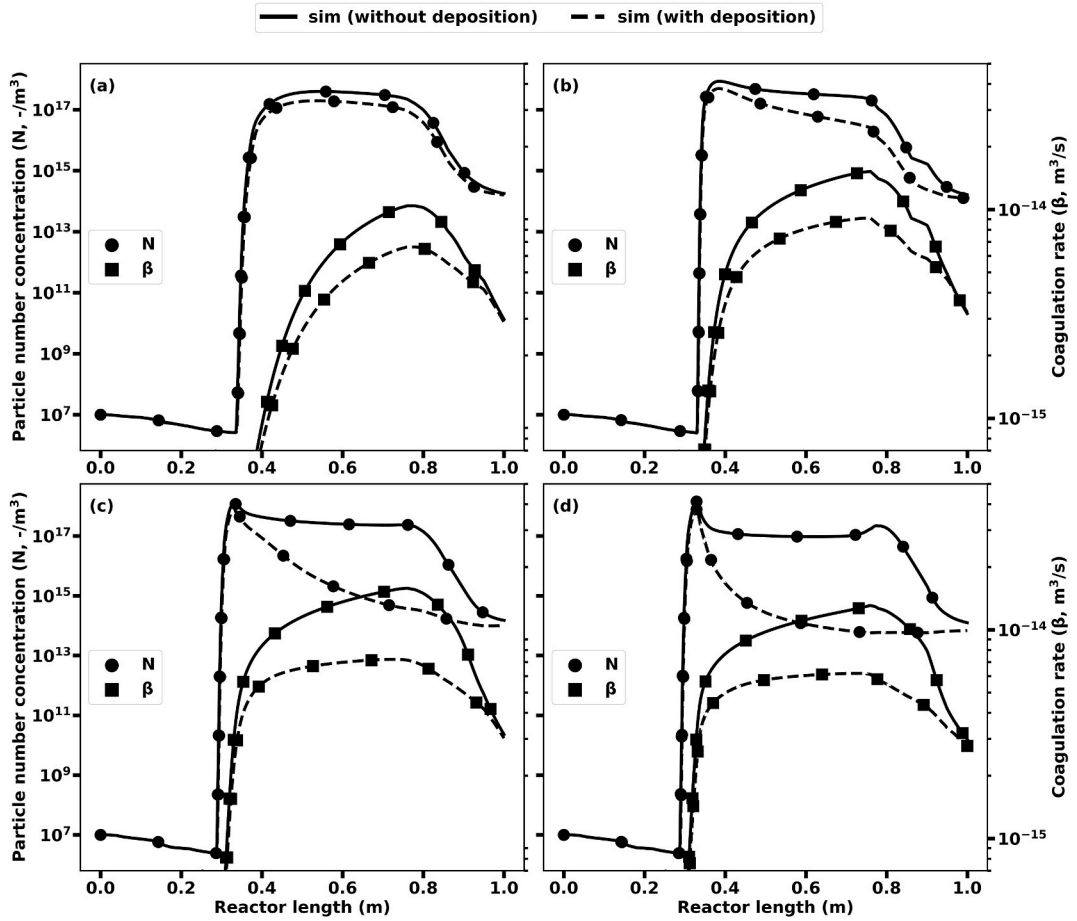

Fig. 6. Total particle (aggregate) number concentration (primary y-axis) and coagulation rate (secondary y-axis) along the reactor axis at hot zone temperature of (a) 1473 K, (b) 1573 K, (c) 1673 K, and (d) 1773 K. (A colour version of this figure can be viewed online.)

reaching its peak within 1–3 mm of the hot zone) begins to decrease due to a decrease in $C_{16}H_{10}$ dimer formation rate. This subsequently leads to an increase in the coagulation rate, demonstrating an inverse relationship between particle number concentration and coagulation rate. In the post-hot zone of the reactor, after coagulation rate reaches its peak, both aggregate particle number concentration and coagulation rate starts to decrease, suggesting a complex interdependence rather than a straightforward inverse relationship. The coagulation process is particularly prominent at higher temperatures (Fig. 6(c) and (d)), underscoring the role of thermal energy in facilitating particle collisions and subsequent growth. While the coagulation rates in Fig. 6 may seem relatively constant across varying temperatures, a closer examination reveals that the peak coagulation rates shift closer to the entrance of the hot zone as the temperature increases. This shift indicates enhanced coagulation early in the reactor length at higher temperatures. Additionally, the coagulation rate within the hot zone increases with

temperature, demonstrating the effect of enhanced thermal conditions on particle interactions and growth. However, by the end of the reactor, the coagulation rates at all temperatures converge, reflecting the depletion of available precursors and the saturation of coagulation processes.

On the other hand, simulations incorporating carbon deposition reactions consistently demonstrate a lower particle (aggregate) number concentration and coagulation rate across the entire temperature range. This suggests that surface reactions consume significant gas-phase species, reducing their availability for particle formation and growth and ultimately affecting the dynamics of soot formation. At higher hot zone temperatures, notably at 1673 K (Fig. 6(c)) and 1773 K (Fig. 6(d)), the aggregate particle number concentration profile exhibits a broader along the reactor length, and the decline after the peak is more gradual. This axial profile indicates a balance between nucleation and coagulation processes due to the increased thermal motion of particles that counteracts coagulation. The corresponding coagulation rate at this high temperature rises less sharply, suggesting a reduced rate of particle aggregation. As the gas progresses along the reactor length to the post-hot zone, both total aggregate particle number concentration and coagulation rate decline, illustrating the depletion of reactive gas-phase species (Fig. 4) and a lesser chance of soot particle aggregation.

It is important to note that while the current model provides valuable insights into the trends and behaviors of soot formation, it is limited in its scope. Using $C_{16}H_{10}$ dimers as a proxy for soot inception simplifies the complex nucleation process and does not account for the potential contributions of reactive intermediates or detailed molecular interactions affecting particle size distribution and growth kinetics.

In addition to the mere particle (aggregate) number concentration, the evolution of the primary particle diameter along the reactor length, is a critical aspect of soot formation and growth as well. Fig. 7 presents the change in the primary particle diameter for the different hot zone temperatures subject to this study. The data (Fig. 7) illustrate the effects of thermal conditions and carbon deposition reactions on particle growth. In both scenarios, at the lower hot zone temperature of 1473 K (Fig. 7(a)), the growth of the primary particle diameter is gradual: it begins to increase partway through the reactor. This suggests that initially nucleation is the dominant process in the first part of the reactor, whereas particle growth through coagulation and surface growth become more significant further along the reactor length (Fig. 6). As the hot zone temperature rises to 1573 K (Fig. 7(b)) and beyond (Fig. 7(c) and (d)), the primary particle diameter experiences a more significant increase at the entrance of the hot zone. This indicates that higher temperatures accelerate the processes contributing to particle growth (coagulation and surface reactions). The impact of wall-carbon deposition reactions on primary particle growth varies with temperature. At lower temperatures, such as 1473 K (Fig. 7(a)) and 1573 K (Fig. 7(b)), the growth of primary particles is similar in both scenarios (with and without carbon deposition) up to a certain point (end of hot zone). However, towards the end of the reactor (post-hot zone), the simulation without carbon deposition shows higher growth of soot particles because gas-phase precursors remain available, allowing particles to continue growing. In contrast, at higher temperatures (1673 K and 1773 K; Fig. 7(c) and (d)), simulations with carbon deposition reactions on reactor wall show a higher initial growth in the hot zone due to rapid surface growth facilitated by deposition reactions. Nevertheless, in the post-hot zone region, the growth rate in simulations without carbon deposition overtakes that with deposition, as more

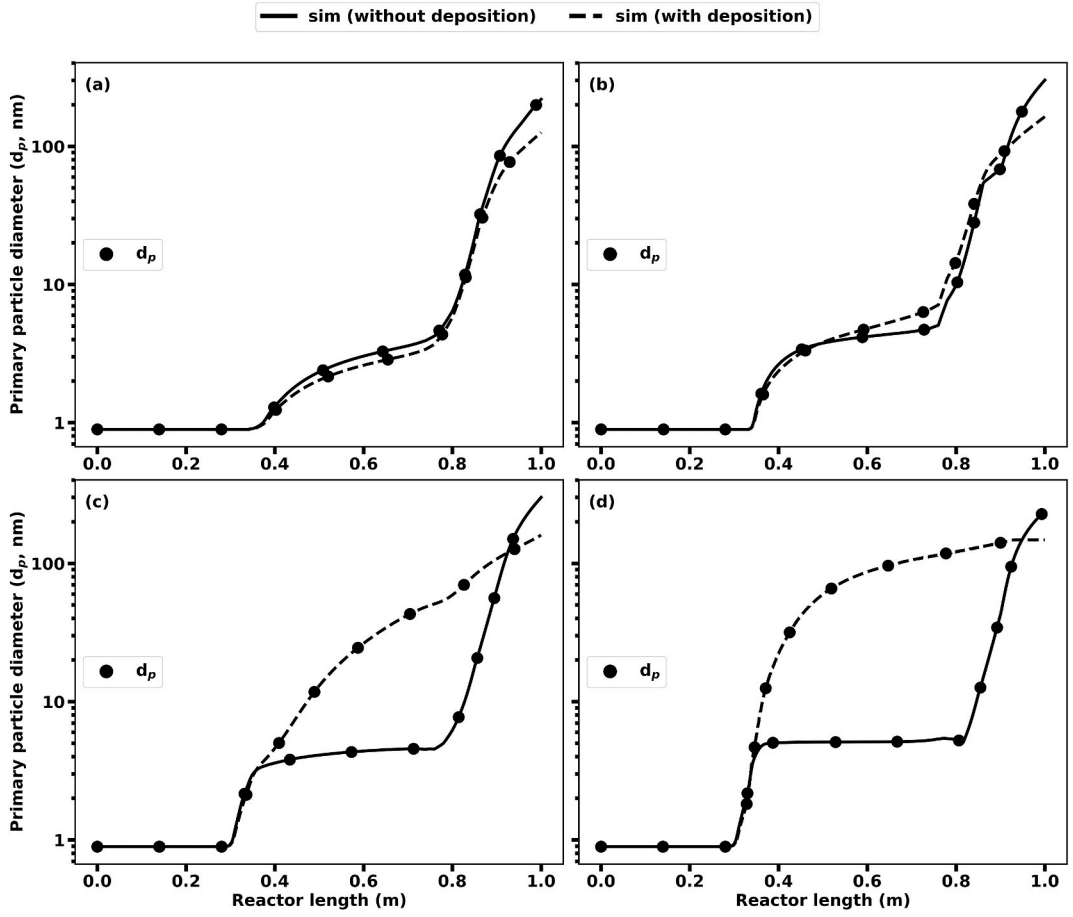

Fig. 7. Evolution of primary particle diameter along the reactor axis at hot zone temperature of (a) 1473 K, (b) 1573 K, (c) 1673 K, and (d) 1773 K. (A colour version of this figure can be viewed online.)

precursors are available in the gas phase for continued particle growth. This trend aligns with the observation that carbon deposition reactions (on reactor wall) consume gas-phase precursor species (Fig. 4), reducing the number of species available for particle growth in the gas phase. Furthermore, this behavior can be attributed to the dynamic equilibrium between the different processes of soot formation (nucleation, coagulation, and surface growth) at such high temperatures. It also suggests that the particles are reaching a size where growth rates may be limited by diffusion and other mass transport processes. Throughout the reactor length, the primary particle diameter increases with the progression of the gas through the hot zone. This observation aligns with the notion that as the gas-phase reactants are consumed and transformed into particulate matter, the particles will increase in size through coagulation and surface accretion processes. Additionally, the carbon deposition reactions notably limit the growth of primary particle diameters in CH_4 pyrolysis. This reduction in particle size due to carbon deposition suggests a significant consumption of reactive hydrocarbons that would otherwise contribute to particle growth and underscores the intricate interplay of kinetic processes that govern the formation and evolution of soot in high-temperature environments.

Correlating the quantitative data from simulations (Fig. 8) with TEM analysis (Fig. 9) of soot samples obtained during experimental measurement allows a detailed comparison of primary particle diameters across hot zone temperatures in CH_4 pyrolysis. To ensure statistical reliability, at least 50 particles were measured at each temperature using ImageJ software to determine the average particle diameters presented in Fig. 8. At 1473 K, Fig. 8, in absence of carbon deposition reaction, simulated particle diameter of 219 nm shows good agreement with the diameter of 205 nm determined by the TEM (Fig. 9(a)). This indicates that carbon deposition may not significantly impede particle growth at a lower temperature (1473 K), as also suggested by the comparable simulated primary particle diameter of 126 nm that is predicted by simulations that take carbon deposition into account. However, as the hot zone temperature increases to 1573 K (Fig. 9(b)), 1673 K (Fig. 9(c)), and 1773 K (Fig. 9(d)), simulations that incorporate carbon deposition reactions show better agreement with TEM results, as shown in Fig. 8. The simulation with deposition reactions yields primary diameters of 164 nm, 160 nm, and 148 nm, respectively, while TEM shows particles at 160 nm, 145 nm, and 130 nm. The simulated values fall well within the experimental error margins, particularly at the higher temperature, underscores that the simulation is capable of accounting for carbon deposition factor in CH_4 pyrolysis process.

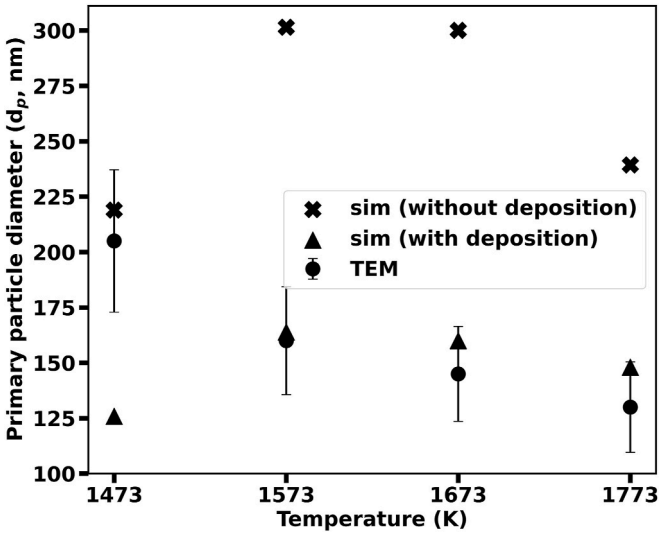

Fig. 8. Comparison of simulated primary particle diameter (with and without wall-carbon deposition reactions) with TEM at hot zone temperature of (a) 1473 K, (b) 1573 K, (c) 1673 K, and (d) 1773 K. (A colour version of this figure can be viewed online.)

The trend of decreasing primary particle diameters with increasing temperature highlights the enhancing effect of higher temperatures on the rate of carbon deposition reactions (Fig. 8). This, in turn, more effectively inhibits particle growth. The measured and predicted data underscores that such deposition reactions are a significant factor in soot particle growth inhibition as temperatures rise, a factor that simulations without consideration of direct carbon deposition reactions fail to capture. Moreover, an agglomeration of the soot particles can be observed in the TEM images (Figs. S2–S5). At 1473 K (Fig. S2), particles appear more isolated, which suggest less prevalent conditions for agglomeration, potentially due to the lower surface mobility of the carbonaceous material. As the temperature increases, particles are in closer proximity and form larger agglomerates (Figs. S3 and S4), indicating enhanced surface activity and interaction between particles. At 1773 K (Fig. S5), the prevalence of agglomerated structures is significantly higher, corroborating the simulation (Fig. 6) data that higher temperatures facilitate more rapid and more extensive agglomeration processes. Simulations closely match TEM measurements for primary particle diameters at higher temperatures, though discrepancies at lower temperatures suggest gaps in capturing all soot inception mechanisms [54]. Thus, predictions for primary particle size should be viewed as indicative of general trends rather than exact values.

The simulated log-normal particle size distributions (PSD), presented in Fig. 10, illustrate the evolution of soot particle sizes as a function of the hot zone temperatures. Without taking wall-carbon deposition reactions into account (Fig. 10(a)), the PSD peaks suggest a temperature-dependent growth of soot particles. This is demonstrated by the shift towards larger diameters from 1473 K to 1673 K, indicating temperature-enhanced nucleation and aggregation. However, at 1773 K, the peak diameter decreases significantly due to a reduced formation of $C_{16}H_{10}$ dimers, which limits available soot precursors due to a predominant conversion of CH_4 to H_2. The narrowing of the PSD at 1473 K (Fig. 10(a)) compared to broader distribution at higher temperatures can be attributed to the dominance of nucleation over coagulation and surface growth at lower temperature. At 1473 K, the thermal energy is insufficient to drive significant coagulation, leading to the formation of smaller, more uniform particles, hence the narrower distribution. As the temperature increases to 1573 K, the coagulation and surface growth mechanism broaden the distribution. With further increase in temperature, the rapid consumption of soot precursors limits the formation of soot dimer, resulting in a narrower distribution, though not as narrow as 1473 K, as larger particles still dominate the PSD due to enhance growth of existing particles. In contrast, simulations incorporating carbon deposition (Fig. 10(b)) predict a different trend, with initial PSD peaks at 1473 K that indicate underestimated particle sizes. This underestimation is attributed to the higher-than-observed consumption rate of C_2H_2 impacting the surface growth of particles. As the temperature rises to 1573 K, the peak shifts to larger diameters, indicating better alignment with the TEM data. At 1673 K, there is a slight shift towards smaller particle sizes. At 1773 K, the PSD peak moves to smaller diameters, highlighting the intensified effect of carbon deposition reactions on reactor wall at high temperatures that limit particle growth due to the competitive consumption of hydrocarbons (C_2H_2, C_2H_4, C_2H_6, C_4H_6, and C_6H_6) on surfaces, which otherwise contribute to the growth of soot particles in the gas phase.

This study uses a one-dimensional plug flow reactor model combined with the method of moments to analyze soot formation in CH_4 pyrolysis, acknowledging its limitations in capturing complex dynamics, particularly near reactor walls where radial effects and carbon deposition occur [69]. As a result, the model may not fully capture all the dynamics involved in particle formation and growth. While the model effectively tracks soot particle size and number density, it does not explicitly address particle maturity, which involves the chemical and structural evolution of soot particles over time [134,135]. Future studies should consider more sophisticated 2D [69,87,90,91] or 3D [89,93] models to

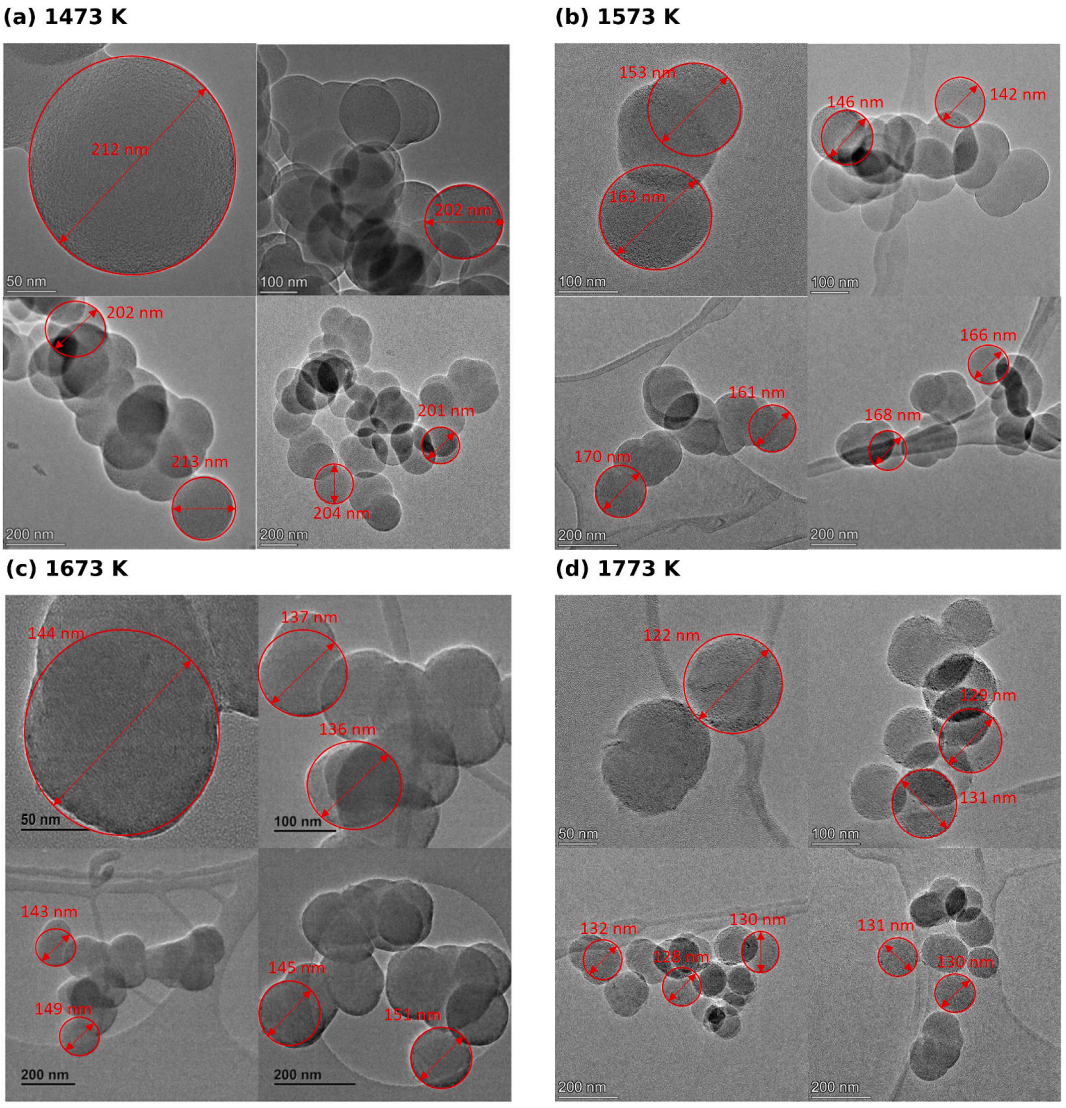

Fig. 9. TEM image analysis of soot samples (primary particle diameter) at hot zone temperature of (a) 1473 K, (b) 1573 K, (c) 1673 K, and (d) 1773 K. (A colour version of this figure can be viewed online.)

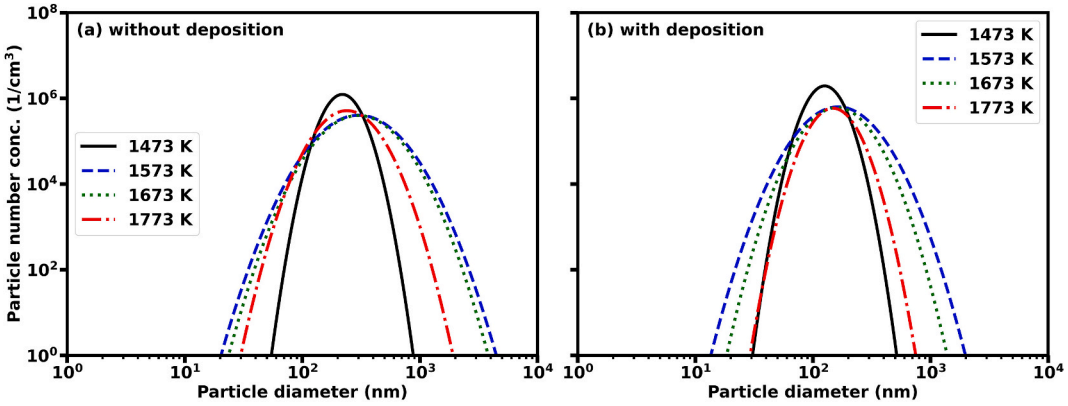

Fig. 10. Log-normal particle size distribution at hot zone temperature of (a) 1473 K, (b) 1573 K, (c) 1673 K, and (d) 1773 K. (A colour version of this figure can be viewed online.)

account for these effects and provide a more accurate representation of soot formation dynamics in methane pyrolysis reactors. While the model incorporates HACA and direct carbon deposition reactions, recent studies [38,52,54,129] indicate additional pathways, such as CHRCR [52], may also play crucial roles in soot formation through resonance-stabilized radical clusters. The relative importance of these

pathways in CH_4 pyrolysis remains uncertain, underscoring the need for further experimental and theoretical studies. Future research should also aim to refine the model by incorporating the dynamics of particle maturity and distinguishing between different soot formation pathways to better evaluate their contributions. Although this study offers an initial understanding of the impact of carbon deposition reactions on soot formation, further investigation is needed for a more comprehensive understanding.

4.4. Characterization results

In addition to the TEM analysis of the soot samples produced at different hot zone temperature were comprehensively analyzed by means of Raman spectroscopy and DLS.

Raman spectroscopy provides information on the structural characteristics of carbonaceous materials. Specifically, the D and G bands shed light on the deviations from perfect graphite structures and the nature of carbon bonding. Fig. 11 depicts the Raman spectra for soot samples produced at varying temperatures (1473 K, 1573 K, 1673 K and 1773 K) and deconvoluted Raman spectra for the soot produced at 1773 K. In Raman analysis, soot signatures typically include the D_3 and D_4 bands, which have been associated with amorphous components and sp3 bonds, respectively [96]. The diminishing intensity of these "soot" bands (D_3 and D_4) as the production temperature increases indicates an improvement in the structural order properties of carbon particles formed in the higher-temperature regime (Fig. 11(a) and (b)).

The D and G bands are central to soot analysis. The G band corresponds to the stretching modes of all sp2 bond pairs and is prominent feature in the first-order region for perfect graphite, which is due to an ideal graphite lattice. In contrast, the D band arises from the motion of sp2-bonded carbon in 6-member rings and is observed in lattices that deviate from perfect graphite structures [136]. A notable observation in this study is the broader full width at half maximum (FWHM) for the D peak compared to the G peak as observed for soot samples produced at lower temperatures. As reaction temperature increases, the D peak narrows, indicating enhanced structural order in the soot sample (Fig. 11(a)). A similar trend was observed for soot formed at flame temperatures above 1950 K [137].

Amorphous carbon and most soot samples, on the other hand, results in broad signals within approximately 2300 cm^{-1} to 3300 cm^{-1} (the second-order region) [96]. Cuesta et al. [138] attribute these signals to second-order bands, overtones, and combinations of graphitic lattice vibration modes. In Fig. 11(b), peaks at 2700 cm^{-1} and 2900 cm^{-1} are ascribed to the (2*D) overtone and (G+D) combination, respectively. In this study, as temperatures surpassed 1573 K, these secondary peaks became sharper, indicating enhanced structural order (Fig. 11(a)). For ideal graphitic material, the D+G peak dominates, with the 2*D band as a shoulder. In contrast, disordered graphite (sp2 carbon material) showcases a stronger 2*D band than the D+G band. This observed evolution of the Raman spectroscopic signature with temperature underscores the transition of carbon from typical soot to a low-defect sp2 carbon structure.

These results align with previous studies [135,139–141] on soot formation and graphitization, where increasing temperatures lead to reduced defects, enhanced structural order, and increased graphitic content [142]. This transformation is captured by the decreasing intensity ratio of the D band to the G band (I_D/I_G), a key metric for assessing soot maturity [139,143]. The sharpening of second-order bands, along with the narrowing of the D band, further supports the transition to a more graphitic structure. Raman spectroscopy helps in assessing soot maturity by providing insights into the structural evolution from amorphous to graphitic carbon with rising temperatures. The I_D/I_G ratio, combined with the analysis of second-order peaks, offers both quantitative and qualitative measures of the soot's structural order and defect density. The results observed in this study are consistent with the current understanding of soot maturation [38,142] and highlight the utility of Raman spectroscopy in elucidating the complex dynamics of carbon structure development at elevated temperatures.

DLS was employed to analyze the size distribution of soot samples produced at different temperatures, as illustrated in Fig. 12. The analysis reveals a distinct pattern: Soot generated at a lower temperature (1473 K) exhibits a more uniform size distribution, devoid of larger aggregate

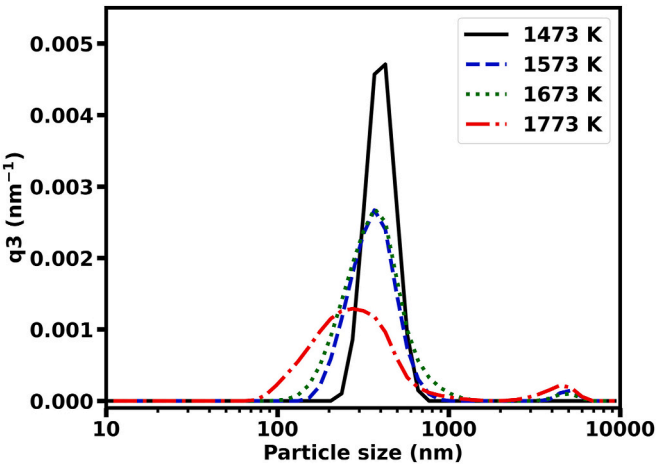

Fig. 12. Density size distribution by intensity of soot samples at hot zone temperature of 1473 K, 1573 K, 1673 K, and 1773 K. (A colour version of this figure can be viewed online.)

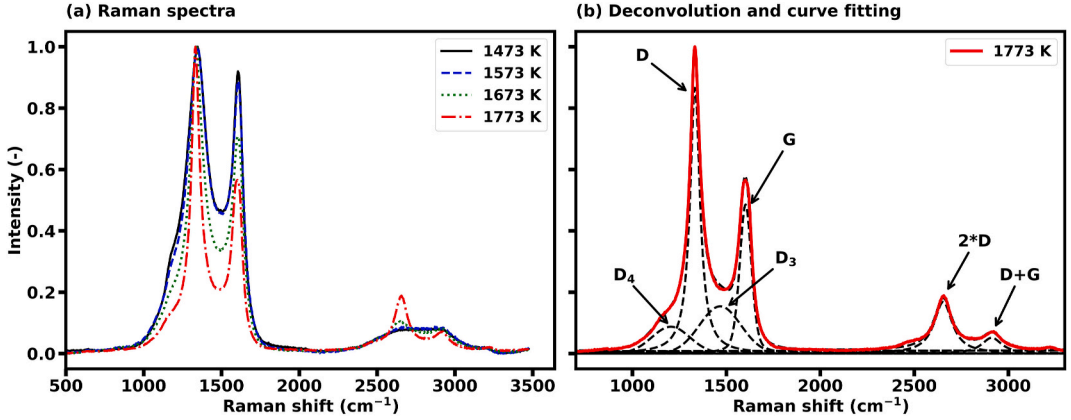

Fig. 11. Raman spectra of soot samples at hot zone temperatures of (a) 1473 K, 1573 K, 1673 K, and 1773 K and (b) detailed deconvolution and curve fitting of Raman spectra at 1773 K. (A colour version of this figure can be viewed online.)

particles. However, as the hot zone temperature increases, the particle size distribution curve broadens as both smaller and larger aggregates are formed. For instance, the soot at 1773 K (represented by the red curve in Fig. 12) exhibits particles ranging from a mere 100 nm to a size of 4000 nm. Detailed data regarding the density distribution depicted in Fig. 12 can be found in Table S3. It can be observed that the aggregate size does not vary significantly if the process temperatures are low. However, at higher temperatures, aggregate size growth is non-uniform, with some aggregates becoming larger while others remain small. Notably, for samples produced at temperatures exceeding 1473 K, a second peak emerges in the density size distribution, whose intensity increases with rising temperature. The median aggregate diameters, as inferred from the cumulative size distribution, for the respective temperatures are 386 nm (1473 K), 410 nm (1573 K), 395 nm (1673 K), and 772 nm (1773 K). This underscores a consistent increase in the median aggregate diameter as the hot zone temperature ascends. Furthermore, with rising temperatures, a broadening of the PSDs is observed in both simulations (Fig. 10) and DLS measurements (Fig. 12). This broadening indicates a diversification in particle sizes due to intensified coagulation and agglomeration processes (Figs. S2–S5). Such broadening is especially pronounced in the simulations that consider wall-carbon deposition. The DLS data support this observation as they reflect a more significant variability in particle sizes and validate the competitive dynamics between particle growth and wall-carbon deposition mechanisms at higher temperatures. Thus, the DLS data not only validate the trend observed in the simulations but also reinforces the accuracy of the simulated PSDs in capturing the complex interplay of factors that regulate particle size distributions in soot formation.

While the DLS data provides valuable insights into the size distribution and broadening of soot particles at different temperatures, it is important to note the limitations of the current experimental setup. The setup is designed primarily for high-temperature/high-pressure conditions and only allows for soot particle collection at the reactor exit. As a result, this study does not include soot mass concentration or in situ particle size distribution measurements, which could provide additional insights into the soot formation dynamics [88,144]. Future experimental studies incorporating these measurements would help to further validate the current model and provide a more comprehensive understanding of the processes governing soot formation and growth in methane pyrolysis reactors.

5. Conclusions

The present study intricately combined a one-dimensional plug flow reactor model coupled with the method of moments and experimental investigations to elucidate the mechanisms of soot particle formation and growth in CH_4 pyrolysis. The simulations, incorporating detailed gas-phase chemical kinetics and direct surface deposition reactions, demonstrated consistency with experiments conducted at various hot zone temperatures. While the characterization of soot particles through TEM, DLS, and Raman spectroscopy supported the general trends observed in the simulations, the model primarily serves as an empirical proxy rather than providing comprehensive insight into the underlying physical mechanisms. The results underscore the need for further experimental data and model refinements to enhance the understanding of soot formation dynamics and to ensure the model's reliability under different conditions.

The study demonstrates the significant impact of hot zone temperatures on morphological and structural attributes of soot particles. Raman spectroscopy analyses have revealed a shift from amorphous to more graphitic structures in soot particles as the pyrolysis reactor operation temperature increases, consistent with previous studies that demonstrate the maturation of the soot carbon structure at elevated temperatures. Furthermore, TEM analysis has shown a decrease in primary particle diameters (205 nm–130 nm) as temperature increases (1473 K–1773 K), which suggests that carbon deposition reactions on reactor wall play a more significant role in particle growth than typical nucleation, surface growth, and agglomeration mechanisms. Simulations performed taking direct carbon deposition reactions into account, used to estimate soot particle sizes, match fairly well with TEM data for soot samples produced at 1573 K, 1673 K, and 1773 K but underpredicted the particle size at 1473 K. Conversely, simulations without carbon deposition reactions slightly overestimated particle size at 1473 K, indicating a higher rate of carbon deposition reactions on reactor wall at this temperature, which leads to increased consumption of growth-facilitating hydrocarbons and thus the underprediction of the particle size at 1473 K in simulations with carbon deposition reactions. Additionally, the broadening of the PSD curves with temperature, observed in both simulations and DLS data, supports the hypothesis that higher temperatures induce greater diversity in particle sizes due to intensified coagulation and agglomeration processes.

The implications of this research extend beyond the immediate findings, providing a valuable model for future studies aimed at optimizing soot production and mitigation in CH_4 pyrolysis. The insights provided by the model, in particular axially resolved information on soot and wall-carbon formation and deposition, lead to potential improvements in reactor design, process optimization, and the development of new strategies for managing soot particles. The consistent alignment of simulated PSDs with DLS observations across a range of temperatures underscores the potential for simulations to accurately predict the reactor behavior accurately. Given the limitations of the current soot inception model, further studies are necessary to refine these predictions and incorporate a broader range of chemical pathways and reactive intermediates. Experimental validation, particularly with spatially-resolved in-situ measurements, would greatly enhance the model's accuracy and reliability in predicting soot formation dynamics. Additionally, further refinement of wall-carbon deposition reaction mechanisms is necessary, offering a valuable direction for future studies to improve the predictive capabilities of soot formation models. This research thus opens the door to novel advancements in understanding soot dynamics during CH_4 pyrolysis in flow reactors under industrially relevant conditions.

Supporting information available

The supporting information for the article is available. The supporting information contains: chemical kinetics, correlations, DLS and TEM results.

Abbreviations

ABF	Appel, Bockhorn, and Frenklach
DLS	Dynamic light scattering
HACA	Hydrogen abstraction carbon addition
MOM	Method of moment
PAHs	Polycyclic aromatic hydrocarbons
CHRCR	Clustering of hydrocarbons by radical-chain reactions
PSD	Particle size distribution
TEM	Transmission electron microscopy

List of symbols

Latin symbols

A	Pre-exponential factor	$m^3\ mol^{-1}\ s^{-1}$
A_{s0}	Monomer surface area	m^2
d_d	Effective diameter of dimer	m
$d_{p,soot}$	Soot particle diameter	m
E_A	Activation energy	$kJ\ mol^{-1}$
E_d	Enhancement factor	–
I	Dimensionless nucleation rate	–
I_{nucl}	Soot nucleation rate	$mol\ m^{-3}\ s^{-1}$
K_c	Dimensionless coagulation coefficient	–
k	Rate constant	$m^3\ s^{-1}$
k_B	Boltzmann constant	$m^2\ kg\ s^{-2}\ K^{-1}$
M	Molar mass	$kg\ mol^{-1}$

(continued on next page)

(*continued*)

M_d	Reduced mass of the dimer	kg
M_0	Zeroth moment	m^{-3}
M_1	First moment	$m^3\ m^{-3}$
M_2	Second moment	$m^3\ m^3\ m^{-3}$
m_m	Initial monomer mass	kg
N'	Dimensionless particle (aggregate) number concentration	–
n_{sat}	Monomer concentration at saturation	m^{-3}
P'	Chemically active perimeter per unit length	m
R	Radius of the reactor	m
r_g	Geometric particle radius	m
r_m	Monomer radius	m
$\dot{s}$	Rate of surface phase reaction	mol $m^{-2}\ s^{-1}$
S_g	Set of gas-phase species	–
T	Gas phase temperature	K
u	Gas velocity	m s^{-1}
V_1'	Dimensionless particle volume concentration	–
V_2'	Dimensionless second aerosol volume moment	–
v_g	Geometric mean volume	m^3
W'	Dimensionless soot surface growth rate	–
Y	Mass faction of species	–
z	Reactor axial coordinate	m
Greek symbols		
α	Fraction of surface site available	–
ζ	Dimensionless coagulation coefficient	–
ζ_{FM}	Dimensionless coagulation coefficient in the free molecular	–
ζ_C	Dimensionless coagulation coefficient in the continuum regimes	–
Θ	Dimensionless residence time	–
λ	Gas mean free path	m
ξ	Dimensionless coagulation coefficient	–
ξ_{FM}	Dimensionless coagulation coefficient in the free molecular	–
ξ_C	Dimensionless coagulation coefficient in the continuum regimes	–
ρ	Gas phase density	kg m^{-3}
ρ_{soot}	Soot density	kg m^{-3}
σ_g	Geometric standard deviation	–
τ	Characteristic time for particle growth	s
$\chi_{C_{soot}H}$	Sites per unit surface area of the particles	site m^{-2}
$\dot{\omega}$	Rate of gas phase reaction mol	$m^{-3}\ s^{-1}$

CRediT authorship contribution statement

Akash Bhimrao Shirsath: Writing – original draft, Visualization, Validation, Software, Methodology, Investigation, Formal analysis, Data curation, Conceptualization. **Manas Mokashi:** Writing – review & editing, Investigation, Formal analysis. **Reihaneh Pashminehazar:** Writing – review & editing, Investigation, Formal analysis. **Ahmet Çelik:** Investigation, Formal analysis. **Patrick Lott:** Writing – review & editing, Supervision, Project administration, Formal analysis, Data curation. **Steffen Tischer:** Writing – review & editing, Supervision, Software, Formal analysis. **Jan-Dierk Grunwaldt:** Writing – review & editing, Supervision, Formal analysis, Conceptualization. **Olaf Deutschmann:** Writing – review & editing, Supervision, Resources, Project administration, Funding acquisition, Data curation, Conceptualization.

Declaration of competing interest

The authors declare that they have no known competing financial interests or personal relationships that could have appeared to influence the work reported in this paper.

Acknowledgement

We very much appreciate fruitful discussions and experimental support from C. Janzer and H. Müller (both KIT). The authors gratefully acknowledge funding by the Federal Ministry of Education and Research (BMBF) of Germany, project Me^2H_2 (grant number 03SF0571B). The omegadot software & consulting GmbH is gratefully acknowledged for a cost-free academic license of DETCHEM™. The Institute of Nanotechnology, Karlsruhe Nano Micro Facility at KIT is gratefully acknowledged for TEM analysis. The authors gratefully acknowledge D. Gase, Institute of Thermal Process Engineering, Karlsruhe Institute of Technology, for DLS analysis. The authors also acknowledge Karlsruhe Institute of Technology and DFG for financing the Raman spectrometer system (INST121384/731).

Appendix A. Supplementary data

Supplementary data to this article can be found online at https://doi.org/10.1016/j.carbon.2024.119689.

References

[1] O. Machhammer, A. Bode, W. Hormuth, Financial and ecological evaluation of hydrogen production processes on large scale, Chem. Eng. Technol. 39 (2016) 1185–1193, https://doi.org/10.1002/ceat.201600023.
[2] P. Lott, O. Deutschmann, Heterogeneous chemical reactions—a cornerstone in emission reduction of local pollutants and greenhouse gases, Proc. Combust. Inst. 39 (2023) 3183–3215, https://doi.org/10.1016/j.proci.2022.06.001.
[3] S. Schneider, S. Bajohr, F. Graf, T. Kolb, State of the art of hydrogen production via pyrolysis of natural gas, ChemBioEng Rev. 7 (2020) 150–158, https://doi.org/10.1002/cben.202000014.
[4] L. Chen, G. Msigwa, M. Yang, A.I. Osman, S. Fawzy, D.W. Rooney, P.-S. Yap, Strategies to achieve a carbon neutral society: a review, Environ. Chem. Lett. 20 (2022) 2277–2310, https://doi.org/10.1007/s10311-022-01435-8.
[5] L. Chen, Z. Qi, S. Zhang, J. Su, G.A. Somorjai, Catalytic hydrogen production from methane: a review on recent progress and prospect, Catalysts 10 (2020), https://doi.org/10.3390/catal10080858.
[6] L. Barelli, G. Bidini, F. Gallorini, S. Servili, Hydrogen production through sorption-enhanced steam methane reforming and membrane technology: a review, Energy 33 (2008) 554–570, https://doi.org/10.1016/j.energy.2007.10.018.
[7] J. Horlyck, C. Lawrey, E.C. Lovell, R. Amal, J. Scott, Elucidating the impact of Ni and Co loading on the selectivity of bimetallic NiCo catalysts for dry reforming of methane, Chem. Eng. J. 352 (2018) 572–580, https://doi.org/10.1016/j.cej.2018.07.009.
[8] A. Giehr, L. Maier, S. Angeli, S.A. Schunk, O. Deutschmann, Dry and steam reforming of CH_4 on Co-hexaaluminate: on the formation of metallic Co and its influence on catalyst activity, Ind. Eng. Chem. Res. 59 (2020) 18790–18797, https://doi.org/10.1021/acs.iecr.0c03522.
[9] S. Hanf, S. Angeli, D. Dussol, C. Fritsch, L. Maier, M. Müller, O. Deutschmann, S. A. Schunk, Methane dry reforming, in: G. Stefanidis, A. Stankiewicz (Eds.), Chem. Valoris. Carbon Dioxide, The Royal Society of Chemistry, 2022, https://doi.org/10.1039/9781839167645-00187.
[10] O. Deutschmann, L.D. Schmidt, Two-dimensional modeling of partial oxidation of methane on rhodium in a short contact time reactor, Symp. Combust. 27 (1998) 2283–2291, https://doi.org/10.1016/S0082-0784(98)80078-7.
[11] R. Schwiedernoch, S. Tischer, C. Correa, O. Deutschmann, Experimental and numerical study on the transient behavior of partial oxidation of methane in a catalytic monolith, Chem. Eng. Sci. 58 (2003) 633–642, https://doi.org/10.1016/S0009-2509(02)00589-4.
[12] C. Diehm, O. Deutschmann, Hydrogen production by catalytic partial oxidation of methane over staged Pd/Rh coated monoliths: spatially resolved concentration and temperature profiles, Int. J. Hydrogen Energy 39 (2014) 17998–18004, https://doi.org/10.1016/j.ijhydene.2014.06.094.
[13] O. Deutschmann, L.D. Schmidt, Modeling the partial oxidation of methane in a short-contact-time reactor, AIChE J. 44 (1998) 2465–2477, https://doi.org/10.1002/aic.690441114.
[14] L. Vidas, R. Castro, Recent developments on hydrogen production technologies: state-of-the-art review with a focus on green-electrolysis, Appl. Sci. 11 (2021), https://doi.org/10.3390/app112311363.
[15] L. Lin, Y. Tian, W. Su, Y. Luo, C. Chen, L. Jiang, Techno-economic analysis and comprehensive optimization of anon-sitehydrogen refuelling station system using ammonia: hybrid hydrogen purification with both high H_2 purity and high recovery, Sustain. Energy Fuels 4 (2020) 3006–3017, https://doi.org/10.1039/c9se01111k.
[16] N.Z. Muradov, CO_2-free production of hydrogen by catalytic pyrolysis of hydrocarbon fuel, Energy Fuel 12 (1998) 41–48, https://doi.org/10.1021/ef9701145.
[17] T.I. Korányi, M. Németh, A. Beck, A. Horváth, Recent advances in methane pyrolysis: turquoise hydrogen with solid carbon production, Energies 15 (2022), https://doi.org/10.3390/en15176342.
[18] S.R. Patlolla, K. Katsu, A. Sharafian, K. Wei, O.E. Herrera, W. Mérida, A review of methane pyrolysis technologies for hydrogen production, Renew. Sustain. Energy Rev. 181 (2023) 113323, https://doi.org/10.1016/j.rser.2023.113323.
[19] M.S. Galtsov-Tsientsiala, A.O. Dudoladov, A.V. Grigorenko, M.S. Vlaskin, Study of soot deposits during continuous methane pyrolysis in a corundum tube, Appl. Sci. 13 (2023), https://doi.org/10.3390/app131910817.

[20] M. Dadsetan, K.G. Latham, B. Kumral, M.F. Khan, M. Scott, T. Mitra, A. Naseri, S. Manzoor, E.R. Bobicki, T. Filleter, M. Titirici, M.J. Thomson, Carbon film produced from microwave-driven methane pyrolysis, Carbon Trends 12 (2023) 100283, https://doi.org/10.1016/j.cartre.2023.100283.

[21] M. Dadsetan, M.F. Khan, M. Salakhi, E.R. Bobicki, M.J. Thomson, CO_2-free hydrogen production via microwave-driven methane pyrolysis, Int. J. Hydrogen Energy 48 (2023) 14565–14576, https://doi.org/10.1016/j.ijhydene.2022.12.353.

[22] A.B. Shirsath, M. Mokashi, P. Lott, H. Müller, R. Pashminehazar, T. Sheppard, S. Tischer, L. Maier, J.-D. Grunwaldt, O. Deutschmann, Soot Formation in methane pyrolysis reactor: modeling soot growth and particle characterization, J. Phys. Chem. A 127 (2023) 2136–2147, https://doi.org/10.1021/acs.jpca.2c06878.

[23] P. Lott, M.B. Mokashi, H. Müller, D.J. Heitlinger, S. Lichtenberg, A.B. Shirsath, C. Janzer, S. Tischer, L. Maier, O. Deutschmann, Hydrogen production and carbon capture by gas-phase methane pyrolysis: a feasibility study, ChemSusChem 16 (2023) e202201720, https://doi.org/10.1002/cssc.202201720.

[24] J. Prabowo, L. Lai, B. Chivers, D. Burke, A.H. Dinh, L. Ye, Y. Wang, Y. Wang, L. Wei, Y. Chen, Solid carbon co-products from hydrogen production by methane pyrolysis: current understandings and recent progress, Carbon 216 (2024) 118507, https://doi.org/10.1016/j.carbon.2023.118507.

[25] M. Msheik, S. Rodat, S. Abanades, Methane cracking for hydrogen production: a review of catalytic and molten media pyrolysis, Energies 14 (2021), https://doi.org/10.3390/en14113107.

[26] M. McConnachie, M. Konarova, S. Smart, Literature review of the catalytic pyrolysis of methane for hydrogen and carbon production, Int. J. Hydrogen Energy 48 (2023) 25660–25682, https://doi.org/10.1016/j.ijhydene.2023.03.123.

[27] A. Bhaskar, M. Assadi, H.N. Somehsaraei, Can methane pyrolysis based hydrogen production lead to the decarbonisation of iron and steel industry? Energy Convers. Manag. X 10 (2021) 100079 https://doi.org/10.1016/j.ecmx.2021.100079.

[28] G.A. Von Wald, M.S. Masnadi, D.C. Upham, A.R. Brandt, Optimization-based technoeconomic analysis of molten-media methane pyrolysis for reducing industrial sector CO_2 emissions, Sustain. Energy Fuels 4 (2020) 4598–4613, https://doi.org/10.1039/d0se00427h.

[29] E.B. Agyekum, C. Nutakor, A.M. Agwa, S. Kamel, A critical review of renewable hydrogen production methods: factors affecting their scale-up and its role in future energy generation, Membranes (Basel). 12 (2022), https://doi.org/10.3390/membranes12020173.

[30] F. Liu, C. Shi, X. Guo, Z. He, L. Pan, Z.F. Huang, X. Zhang, J.J. Zou, Rational design of better hydrogen evolution electrocatalysts for water splitting: a review, Adv. Sci. 9 (2022) 2200307, https://doi.org/10.1002/advs.202200307.

[31] A.K. Sarker, A.K. Azad, M.G. Rasul, A.T. Doppalapudi, Prospect of green hydrogen generation from hybrid renewable energy sources: a review, Energies 16 (2023), https://doi.org/10.3390/en16031556.

[32] M.F. Vostakola, B. Salamatinia, B.A. Horri, A review on recent progress in the integrated green hydrogen production processes, Energies 15 (2022), https://doi.org/10.3390/en15031209.

[33] G. Maag, G. Zanganeh, A. Steinfeld, Solar thermal cracking of methane in a particle-flow reactor for the co-production of hydrogen and carbon, Int. J. Hydrogen Energy 34 (2009) 7676–7685, https://doi.org/10.1016/j.ijhydene.2009.07.037.

[34] S.H. Park, S.N. Rogak, W.K. Bushe, J.Z. Wen, M.J. Thomson, An aerosol model to predict size and structure of soot particles, Combust. Theor. Model. 9 (2005) 499–513, https://doi.org/10.1080/13647830500195005.

[35] M. Mokashi, A.B. Shirsath, A. Çelik, P. Lott, H. Müller, S. Tischer, L. Maier, J. Bode, D. Schlereth, F. Scheiff, D. Flick, M. Bender, K. Ehrhardt, O. Deutschmann, Methane pyrolysis in packed bed reactors: kinetic modeling, numerical simulations, and experimental insights, Chem. Eng. J. 485 (2024) 149684, https://doi.org/10.1016/j.cej.2024.149684.

[36] T. Geißler, A. Abánades, A. Heinzel, K. Mehravaran, G. Müller, R.K. Rathnam, C. Rubbia, D. Salmieri, L. Stoppel, S. Stückrad, A. Weisenburger, H. Wenninger, T. Wetzel, Hydrogen production via methane pyrolysis in a liquid metal bubble column reactor with a packed bed, Chem. Eng. J. 299 (2016) 192–200, https://doi.org/10.1016/j.cej.2016.04.066.

[37] S. Kreuznacht, M. Purcel, S. Böddeker, P. Awakowicz, W. Xia, M. Muhler, M. Böke, A. von Keudell, Comparison of the performance of a microwave plasma torch and a gliding arc plasma for hydrogen production via methane pyrolysis, Plasma Process. Polym. 20 (2023) 2200132, https://doi.org/10.1002/ppap.202200132.

[38] M.J. Thomson, Modeling soot formation in flames and reactors: recent progress and current challenges, Proc. Combust. Inst. 39 (2023) 805–823, https://doi.org/10.1016/j.proci.2022.07.263.

[39] J.M. Gebert, B. Reznik, R. Piat, B. Viering, K. Weidenmann, A. Wanner, O. Deutschmann, Elastic constants of high-texture pyrolytic carbon measured by ultrasound phase spectroscopy, Carbon 48 (2010) 3647–3650, https://doi.org/10.1016/j.carbon.2010.06.002.

[40] A. Li, G. Schoch, S. Lichtenberg, D. Zhang, O. Deutschmann, A novel CVD/CVI reactor with an in-situ sampling apparatus connected to an online GC/MS, Surf. Coating. Technol. 201 (2007) 8939–8943, https://doi.org/10.1016/j.surfcoat.2007.05.010.

[41] K. Norinaga, O. Deutschmann, K.J. Hüttinger, Analysis of gas phase compounds in chemical vapor deposition of carbon from light hydrocarbons, Carbon 44 (2006) 1790–1800, https://doi.org/10.1016/j.carbon.2005.12.050.

[42] B. Reznik, K. Norinaga, D. Gerthsen, O. Deutschmann, The effect of cooling rate on hydrogen release from a pyrolytic carbon coating and its resulting morphology, Carbon 44 (2006) 1330–1334, https://doi.org/10.1016/j.carbon.2005.12.014.

[43] A. Becker, K.J. Hüttinger, Chemistry and kinetics of chemical vapor deposition of pyrocarbon - IV pyrocarbon deposition from methane in the low temperature regime, Carbon 36 (1998) 213–224, https://doi.org/10.1016/S0008-6223(97)00177-2.

[44] M. Frenklach, H. Wang, Detailed mechanism and modeling of soot particle formation, in: H. Bockhorn (Ed.), Springer Ser. Chem. Phys., Springer, Berlin Heidelberg, Berlin, Heidelberg, 1994, pp. 165–192, https://doi.org/10.1007/978-3-642-85167-4_10.

[45] G. Fau, N. Gascoin, J. Steelant, Hydrocarbon pyrolysis with a methane focus: a review on the catalytic effect and the coke production, J. Anal. Appl. Pyrolysis 108 (2014) 1–11, https://doi.org/10.1016/j.jaap.2014.05.022.

[46] N. Sánchez-Bastardo, R. Schlögl, H. Ruland, Methane pyrolysis for CO_2-free H_2 production: a green process to overcome renewable energies unsteadiness, Chem.-Ing.-Tech. 92 (2020) 1596–1609, https://doi.org/10.1002/cite.202000029.

[47] P.A. Tesner, S.V. Shurupov, Soot formation during pyrolysis of naphthalene, anthracene and pyrene, Combust. Sci. Technol. 126 (1997) 139–151, https://doi.org/10.1080/00102209708935671.

[48] P.A. Tesner, S.V. Shurupov, Some physico-chemical parameters of soot formation during pyrolysis of hydrocarbons, Combust. Sci. Technol. 105 (1995) 147–161, https://doi.org/10.1080/00102209508907744.

[49] A. Çelik, I. Ben Othman, H. Müller, P. Lott, O. Deutschmann, Pyrolysis of biogas for carbon capture and carbon dioxide-free production of hydrogen, React. Chem. Eng. 9 (2023) 108–118, https://doi.org/10.1039/d3re00360d.

[50] M. Frenklach, Reaction mechanism of soot formation in flames, Phys. Chem. Chem. Phys. 4 (2002) 2028–2037, https://doi.org/10.1039/b110045a.

[51] J. Appel, H. Bockhorn, M. Frenklach, Kinetic modeling of soot formation with detailed chemistry and physics: laminar premixed flames of C2 hydrocarbons, Combust. Flame. 121 (2000) 122–136, https://doi.org/10.1016/S0010-2180(99)00135-2.

[52] K.O. Johansson, M.P. Head-Gordon, P.E. Schrader, K.R. Wilson, H.A. Michelsen, Resonance-stabilized hydrocarbon-radical chain reactions may explain soot inception and growth, Science 361 (2018) 997–1000, https://doi.org/10.1126/science.aat3417.

[53] H. Jin, L. Xing, D. Liu, J. Hao, J. Yang, A. Farooq, First aromatic ring formation by the radical-chain reaction of vinylacetylene and propargyl, Combust. Flame 225 (2021) 524–534, https://doi.org/10.1016/j.combustflame.2020.11.034.

[54] M. Frenklach, A.M. Mebel, On the mechanism of soot nucleation, Phys. Chem. Chem. Phys. 22 (2020) 5314–5331, https://doi.org/10.1039/d0cp00116c.

[55] K.O. Johansson, T. Dillstrom, P. Elvati, M.F. Campbell, P.E. Schrader, D. M. Popolan-Vaida, N.K. Richards-Henderson, K.R. Wilson, A. Violi, H. A. Michelsen, Radical–radical reactions, pyrene nucleation, and incipient soot formation in combustion, Proc. Combust. Inst. 36 (2017) 799–806, https://doi.org/10.1016/j.proci.2016.07.130.

[56] X. Huo, W. Chen, L. Liu, W. Liu, H. Ren, Importance of resonance-stabilized radicals in soot formation mechanism of diphenyl ether pyrolysis, J. Anal. Appl. Pyrolysis 175 (2023) 106196, https://doi.org/10.1016/j.jaap.2023.106196.

[57] J.A. Rundel, K.O. Johansson, P.E. Schrader, R.P. Bambha, K.R. Wilson, J. Zádor, G.B. Ellison, H.A. Michelsen, Production of aliphatic-linked polycyclic hydrocarbons during radical-driven particle formation from propyne and propene pyrolysis, Combust. Flame 258 (2023) 112457, https://doi.org/10.1016/j.combustflame.2022.112457.

[58] A. Nobili, A. Cuoci, W. Pejpichestakul, M. Pelucchi, C. Cavallotti, T. Faravelli, Modeling soot particles as stable radicals: a chemical kinetic study on formation and oxidation. Part I. Soot formation in ethylene laminar premixed and counterflow diffusion flames, Combust. Flame 243 (2022) 112073, https://doi.org/10.1016/j.combustflame.2022.112073.

[59] F. Serse, Z. Ding, M. Bracconi, M. Maestri, A. Nobili, C. Giudici, A. Frassoldati, T. Faravelli, A. Cuoci, M. Pelucchi, A comprehensive kinetic framework for solid carbon deposition and hydrogen production from the pyrolysis of light hydrocarbons streams, Carbon Trends 11 (2023) 100263, https://doi.org/10.1016/j.cartre.2023.100263.

[60] F. Cepeda, L. Di Liddo, M.J. Thomson, Enhancing hydrogen production: modelling the role of activated carbon catalyst in methane pyrolysis, Int. J. Hydrogen Energy 83 (2024) 410–420, https://doi.org/10.1016/j.ijhydene.2024.08.056.

[61] K. Norinaga, O. Deutschmann, Detailed kinetic modeling of gas-phase reactions in the chemical vapor deposition of carbon from light hydrocarbons, Ind. Eng. Chem. Res. 46 (2007) 3547–3557, https://doi.org/10.1021/ie061207p.

[62] A. Li, K. Norinaga, W. Zhang, O. Deutschmann, Modeling and simulation of materials synthesis: chemical vapor deposition and infiltration of pyrolytic carbon, Compos. Sci. Technol. 68 (2008) 1097–1104, https://doi.org/10.1016/j.compscitech.2007.07.007.

[63] A. Li, O. Deutschmann, Transient modeling of chemical vapor infiltration of methane using multi-step reaction and deposition models, Chem. Eng. Sci. 62 (2007) 4976–4982, https://doi.org/10.1016/j.ces.2007.01.069.

[64] J.Z. Wen, M.J. Thomson, M.F. Lightstone, S.H. Park, S.N. Rogak, An improved moving sectional aerosol model of soot formation in a plug flow reactor, Combust. Sci. Technol. 178 (2006) 921–951, https://doi.org/10.1080/00102200500270007.

[65] H. Sabbah, L. Biennier, S.J. Klippenstein, I.R. Sims, B.R. Rowe, Exploring the role of PAHs in the formation of soot: pyrene dimerization, J. Phys. Chem. Lett. 1 (2010) 2962–2967, https://doi.org/10.1021/jz101033t.

[66] X. Mercier, O. Carrivain, C. Irimiea, A. Faccinetto, E. Therssen, Dimers of polycyclic aromatic hydrocarbons: the missing pieces in the soot formation process, Phys. Chem. Chem. Phys. 21 (2019) 8282–8294, https://doi.org/10.1039/C9CP00394K.

[67] D. Chakraborty, H. Lischka, W.L. Hase, Dynamics of pyrene-dimer association and ensuing pyrene-dimer dissociation, J. Phys. Chem. A 124 (2020) 8907–8917, https://doi.org/10.1021/acs.jpca.0c06677.

[68] K. Gleason, F. Carbone, A.J. Sumner, B.D. Drollette, D.L. Plata, A. Gomez, Small aromatic hydrocarbons control the onset of soot nucleation, Combust. Flame 223 (2021) 398–406, https://doi.org/10.1016/j.combustflame.2020.08.029.

[69] N.A. Juan, N.A. Eaves, M.J. Thomson, The effect of radial diffusion on nanoparticle formation in laminar flow reactors, Combust. Flame 236 (2022) 111757, https://doi.org/10.1016/j.combustflame.2021.111757.

[70] M.R. Kholghy, G.A. Kelesidis, S.E. Pratsinis, Reactive polycyclic aromatic hydrocarbon dimerization drives soot nucleation, Phys. Chem. Chem. Phys. 20 (2018) 10925–10938, https://doi.org/10.1039/c7cp07803j.

[71] J.Z. Wen, M.J. Thomson, S.H. Park, S.N. Rogak, M.F. Lightstone, Study of soot growth in a plug flow reactor using a moving sectional model, Proc. Combust. Inst. 30 (2005) 1477–1484, https://doi.org/10.1016/j.proci.2004.08.178.

[72] H.A. Michelsen, M.B. Colket, P.-E. Bengtsson, A. D'Anna, P. Desgroux, B. S. Haynes, J.H. Miller, G.J. Nathan, H. Pitsch, H. Wang, A review of terminology used to describe soot formation and evolution under combustion and pyrolytic conditions, ACS Nano 14 (2020) 12470–12490, https://doi.org/10.1021/acsnano.0c06226.

[73] M.R. Kholghy, G.A. Kelesidis, Surface growth, coagulation and oxidation of soot by a monodisperse population balance model, Combust. Flame 227 (2021) 456–463, https://doi.org/10.1016/j.combustflame.2021.01.010.

[74] A. Kazakov, M. Frenklach, Dynamic modeling of soot particle coagulation and aggregation: implementation with the method of moments and application to high-pressure laminar premixed flames, Combust. Flame 114 (1998) 484–501, https://doi.org/10.1016/S0010-2180(97)00322-2.

[75] S.E. Pratsinis, Simultaneous nucleation, condensation, and coagulation in aerosol reactors, J. Colloid Interface Sci. 124 (1988) 416–427, https://doi.org/10.1016/0021-9797(88)90180-4.

[76] G.A. Kelesidis, E. Goudeli, S.E. Pratsinis, Flame synthesis of functional nanostructured materials and devices: surface growth and aggregation, Proc. Combust. Inst. 36 (2017) 29–50, https://doi.org/10.1016/j.proci.2016.08.078.

[77] G.A. Kelesidis, E. Goudeli, S.E. Pratsinis, Morphology and mobility diameter of carbonaceous aerosols during agglomeration and surface growth, Carbon 121 (2017) 527–535, https://doi.org/10.1016/j.carbon.2017.06.004.

[78] G.A. Kelesidis, M.R. Kholghy, A monodisperse population balance model for nanoparticle agglomeration in the transition regime, Materials 14 (2021) 3882, https://doi.org/10.3390/ma14143882.

[79] S. Tsantilis, S.E. Pratsinis, Soft- and hard-agglomerate aerosols made at high temperatures, Langmuir 20 (2004) 5933–5939, https://doi.org/10.1021/la036389w.

[80] F.E. Kruis, K.A. Kusters, S.E. Pratsinis, B. Scarlett, A simple model for the evolution of the characteristics of aggregate particles undergoing coagulation and sintering, Aerosol Sci. Technol. 19 (1993) 514–526, https://doi.org/10.1080/02786829308959656.

[81] E.K.Y. Yapp, D. Chen, J. Akroyd, S. Mosbach, M. Kraft, J. Camacho, H. Wang, Numerical simulation and parametric sensitivity study of particle size distributions in a burner-stabilised stagnation flame, Combust. Flame 162 (2015) 2569–2581, https://doi.org/10.1016/j.combustflame.2015.03.006.

[82] M. Frenklach, S.J. Harris, Aerosol dynamics modeling using the method of moments, J. Colloid Interface Sci. 118 (1987) 252–261, https://doi.org/10.1016/0021-9797(87)90454-1.

[83] A. Naseri, M.R. Kholghy, N.A. Juan, M.J. Thomson, Simulating yield and morphology of carbonaceous nanoparticles during fuel pyrolysis in laminar flow reactors enabled by reactive inception and aromatic adsorption, Combust. Flame 237 (2022), https://doi.org/10.1016/j.combustflame.2021.111721.

[84] M. Balthasar, M. Kraft, A stochastic approach to calculate the particle size distribution function of soot particles in laminar premixed flames, Combust. Flame 133 (2003) 289–298, https://doi.org/10.1016/S0010-2180(03)00003-8.

[85] J. Appel, H. Bockhorn, M. Wulkow, A detailed numerical study of the evolution of soot particle size distributions in laminar premixed flames, Chemosphere 42 (2001) 635–645, https://doi.org/10.1016/S0045-6535(00)00237-X.

[86] M. Frenklach, H. Wang, Detailed modeling of soot particle nucleation and growth, Symp. Combust. 23 (1991) 1559–1566, https://doi.org/10.1016/S0082-0784(06)80426-1.

[87] D. Zheng, A. Nobili, A. Cuoci, M. Pelucchi, X. Hui, T. Faravelli, Soot formation from n-heptane counterflow diffusion flames: two-dimensional and oxygen effects, Combust. Flame 258 (2023) 112441, https://doi.org/10.1016/j.combustflame.2022.112441.

[88] A. Eveleigh, N. Ladommatos, R. Balachandran, Gas and particulate matter products formed in a laminar flow reactor: pyrolysis of single-component C2 fuels, Energy Proc. 66 (2015) 41–44, https://doi.org/10.1016/j.egypro.2015.02.022.

[89] B. Wang, S. Mosbach, S. Schmutzhard, S. Shuai, Y. Huang, M. Kraft, Modelling soot formation from wall films in a gasoline direct injection engine using a detailed population balance model, Appl. Energy 163 (2016) 154–166, https://doi.org/10.1016/j.apenergy.2015.11.011.

[90] R.I.A. Patterson, M. Kraft, Models for the aggregate structure of soot particles, Combust. Flame 151 (2007) 160–172, https://doi.org/10.1016/j.combustflame.2007.04.012.

[91] L. Henderson, P. Shukla, V. Rudolph, S.K. Bhatia, Modelling the formation, growth and coagulation of soot in a combustion system using a 2-D population balance model, Combust. Flame 245 (2022) 112303, https://doi.org/10.1016/j.combustflame.2022.112303.

[92] A. Naseri, M.J. Thomson, Development of a numerical model to simulate carbon black synthesis and predict the aggregate structure in flow reactors, Combust. Flame 207 (2019) 314–326, https://doi.org/10.1016/j.combustflame.2019.06.001.

[93] S. Hong, M.S. Wooldridge, H.G. Im, D.N. Assanis, H. Pitsch, Development and application of a comprehensive soot model for 3D CFD reacting flow studies in a diesel engine, Combust. Flame 143 (2005) 11–26, https://doi.org/10.1016/j.combustflame.2005.04.007.

[94] S.D. Angeli, S. Gossler, S. Lichtenberg, G. Kass, A.K. Agrawal, M. Valerius, K. P. Kinzel, O. Deutschmann, Reduction of CO_2 emission from off-gases of steel industry by dry reforming of methane, Angew. Chem. Int. Ed. 60 (2021) 11852–11857, https://doi.org/10.1002/anie.202100577.

[95] A. Böttcher, F. Hennrich, H. Rösner, S. Malik, M.M. Kappes, S. Lichtenberg, G. Schoch, O. Deutschmann, Growth of novel carbon phases by methane infiltration of free-standing single-walled carbon nanotube films, Carbon 45 (2007) 1085–1096, https://doi.org/10.1016/j.carbon.2006.12.008.

[96] A. Sadezky, H. Muckenhuber, H. Grothe, R. Niessner, U. Pöschl, Raman microspectroscopy of soot and related carbonaceous materials: spectral analysis and structural information, Carbon 43 (2005) 1731–1742, https://doi.org/10.1016/j.carbon.2005.02.018.

[97] L. Bokobza, J.-L. Bruneel, M. Couzi, Raman spectra of carbon-based materials (from graphite to carbon black) and of some silicone composites, C 1 (2015) 77–94, https://doi.org/10.3390/c1010077.

[98] M. Mokashi, A.B. Shirsath, P. Lott, H. Müller, S. Tischer, L. Maier, O. Deutschmann, Understanding of gas-phase methane pyrolysis towards hydrogen and solid carbon with detailed kinetic simulations and experiments, Chem. Eng. J. 479 (2024) 147556, https://doi.org/10.1016/j.cej.2023.147556.

[99] Q. Mao, A.C.T. van Duin, K.H. Luo, Formation of incipient soot particles from polycyclic aromatic hydrocarbons: a ReaxFF molecular dynamics study, Carbon 121 (2017) 380–388, https://doi.org/10.1016/j.carbon.2017.06.009.

[100] T.S. Totton, A.J. Misquitta, M. Kraft, A quantitative study of the clustering of polycyclic aromatic hydrocarbons at high temperatures, Phys. Chem. Chem. Phys. 14 (2012) 4081–4094, https://doi.org/10.1039/C2CP23008A.

[101] P. Elvati, A. Violi, Thermodynamics of poly-aromatic hydrocarbon clustering and the effects of substituted aliphatic chains, Proc. Combust. Inst. 34 (2013) 1837–1843, https://doi.org/10.1016/j.proci.2012.07.030.

[102] H. Wang, Formation of nascent soot and other condensed-phase materials in flames, Proc. Combust. Inst. 33 (2011) 41–67, https://doi.org/10.1016/j.proci.2010.09.009.

[103] W. Pejpichestakul, E. Ranzi, M. Pelucchi, A. Frassoldati, A. Cuoci, A. Parente, T. Faravelli, Examination of a soot model in premixed laminar flames at fuel-rich conditions, Proc. Combust. Inst. 37 (2019) 1013–1021, https://doi.org/10.1016/j.proci.2018.06.104.

[104] G. Blanquart, P. Pepiot-Desjardins, H. Pitsch, Chemical mechanism for high temperature combustion of engine relevant fuels with emphasis on soot precursors, Combust. Flame 156 (2009) 588–607, https://doi.org/10.1016/j.combustflame.2008.12.007.

[105] F. Liu, Y. Ai, W. Kong, Effect of hydrogen and helium addition to fuel on soot formation in an axisymmetric coflow laminar methane/air diffusion flame, Int. J. Hydrogen Energy 39 (2014) 3936–3946, https://doi.org/10.1016/j.ijhydene.2013.12.151.

[106] Q. Zhang, H. Guo, F. Liu, G.J. Smallwood, M.J. Thomson, Modeling of soot aggregate formation and size distribution in a laminar ethylene/air coflow diffusion flame with detailed PAH chemistry and an advanced sectional aerosol dynamics model, Proc. Combust. Inst. 32 I (2009) 761–768, https://doi.org/10.1016/j.proci.2008.06.109.

[107] F. Liu, X. He, X. Ma, Q. Zhang, M.J. Thomson, H. Guo, G.J. Smallwood, S. Shuai, J. Wang, An experimental and numerical study of the effects of dimethyl ether addition to fuel on polycyclic aromatic hydrocarbon and soot formation in laminar coflow ethylene/air diffusion flames, Combust. Flame 158 (2011) 547–563, https://doi.org/10.1016/j.combustflame.2010.10.005.

[108] T. Mitra, C. Chu, A. Naseri, M.J. Thomson, Polycyclic aromatic hydrocarbon formation in a flame of the alkylated aromatic trimethylbenzene compared to those of the alkane dodecane, Combust. Flame 223 (2021) 495–510, https://doi.org/10.1016/j.combustflame.2020.10.015.

[109] N.A. Eaves, S.B. Dworkin, M.J. Thomson, The importance of reversibility in modeling soot nucleation and condensation processes, Proc. Combust. Inst. 35 (2015) 1787–1794, https://doi.org/10.1016/j.proci.2014.05.036.

[110] S. Macadam, J.M. Beér, A.F. Safofim, A.B. Hoffmann, Soot surface growth by polycyclic aromatic hydrocarbon and acetylene addition, Symp. Combust. 26 (1996) 2295–2302, https://doi.org/10.1016/S0082-0784(96)80057-9.

[111] M. Salakhi, F. Cepeda, M.J. Thomson, A comprehensive kinetic study on low-GHG hydrogen production from microwave-driven methane pyrolysis, Int. J. Hydrogen Energy 77 (2024) 997–1008, https://doi.org/10.1016/j.ijhydene.2024.06.259.

[112] K.J. Hüttinger, CVD in hot wall reactors - the interaction between homogeneous gas-phase and heterogeneous surface reactions, Chem. Vap. Depos. 4 (1998) 151–158, https://doi.org/10.1002/(sici)1521-3862(199807)04:04<151::aid-cvde151>3.0.co;2-2.

[113] W. Benzinger, A. Becker, K.J. Hüttinger, Chemistry and kinetics of chemical vapour deposition of pyrocarbon: I. Fundamentals of kinetics and chemical reaction engineering, Carbon 34 (1996) 957–966, https://doi.org/10.1016/0008-6223(96)00010-3.
[114] A. Çelik, A.B. Shirsath, F. Syla, H. Müller, P. Lott, O. Deutschmann, On the role of hydrogen inhibition in gas-phase methane pyrolysis for carbon capture and hydrogen production in a tubular flow reactor, J. Anal. Appl. Pyrolysis 181 (2024) 106628, https://doi.org/10.1016/j.jaap.2024.106628.
[115] A. Becker, Z. Hu, K.J. Hüttinger, Hydrogen inhibition model of carbon deposition from light hydrocarbons, Fuel 79 (2000) 1573–1580, https://doi.org/10.1016/S0016-2361(00)00030-2.
[116] S. Wan, K. Keller, P. Lott, A.B. Shirsath, S. Tischer, T. Häber, R. Suntz, O. Deutschmann, Experimental and numerical investigation of NO oxidation on Pt/Al_2O_3- and NOx storage on $Pt/BaO/Al_2O_3$-catalysts, Catal. Sci. Technol. 12 (2022) 4456–4470, https://doi.org/10.1039/d2cy00572g.
[117] A.B. Shirsath, M.L. Schulte, B. Kreitz, S. Tischer, J.-D. Grunwaldt, O. Deutschmann, Spatially-resolved investigation of CO_2 methanation over $Ni/\gamma\text{-}Al_2O_3$ and $Ni_{3.2}Fe/\gamma\text{-}Al_2O_3$ catalysts in a packed-bed reactor, Chem. Eng. J. 469 (2023) 143847, https://doi.org/10.1016/j.cej.2023.143847.
[118] P. Deuflhard, E. Hairer, J. Zugck, One-step and extrapolation methods for differential-algebraic systems, Numer. Math. 51 (1987) 501–516, https://doi.org/10.1007/BF01400352.
[119] R.B. Bird, W.E. Stewart, E.N. Lightfoot, Transport Phenomena, Wiley, 2006.
[120] T.L. Bergman, A.S. Lavine, F.P. Incropera, D.P. DeWitt, Introduction to Heat Transfer, John Wiley & Sons, 2011.
[121] H. Zhang, G. Sharma, S. Dhawan, D. Dhanraj, Z. Li, P. Biswas, Comparison of discrete, discrete-sectional, modal and moment models for aerosol dynamics simulations, Aerosol Sci. Technol. 54 (2020) 739–760, https://doi.org/10.1080/02786826.2020.1723787.
[122] R.F. Kulakhmetov, T.L. Pourpoint, 1D plug flow reactor modeling approach of soot formation and deposition in a fuel rich kerosene combustor, in: AIAA Scitech 2020 Forum, American Institute of Aeronautics and Astronautics, 2020, https://doi.org/10.2514/6.2020-1428.
[123] M. Balthasar, F. Mauss, A. Knobel, M. Kraft, Detailed modeling of soot formation in a partially stirred plug flow reactor, Combust. Flame 128 (2002) 395–409, https://doi.org/10.1016/S0010-2180(01)00344-3.
[124] M. Frenklach, Method of moments with interpolative closure, Chem. Eng. Sci. 57 (2002) 2229–2239, https://doi.org/10.1016/S0009-2509(02)00113-6.
[125] V. Chernov, M.J. Thomson, S.B. Dworkin, N.A. Slavinskaya, U. Riedel, Soot formation with C1 and C2 fuels using an improved chemical mechanism for PAH growth, Combust. Flame 161 (2014) 592–601, https://doi.org/10.1016/j.combustflame.2013.09.017.
[126] S.H. Park, K.W. Lee, E. Otto, H. Fissan, The log-normal size distribution theory of brownian aerosol coagulation for the entire particle size range: Part I—analytical solution using the harmonic mean coagulation kernel, J. Aerosol Sci. 30 (1999) 3–16, https://doi.org/10.1016/S0021-8502(98)00037-8.
[127] S. Liu, T.L. Chan, J. Lin, M. Yu, Numerical study on fractal-like soot aggregate dynamics of turbulent ethylene-oxygen flame, Fuel 256 (2019) 115857, https://doi.org/10.1016/j.fuel.2019.115857.
[128] A. Holmen, O. Olsvik, O.A. Rokstad, Pyrolysis of natural gas: chemistry and process concepts, Fuel Process. Technol. 42 (1995) 249–267, https://doi.org/10.1016/0378-3820(94)00109-7.
[129] J.A. Rundel, C.M. Thomas, P.E. Schrader, K.R. Wilson, K.O. Johansson, R. P. Bambha, H.A. Michelsen, Promotion of particle formation by resonance-stabilized radicals during hydrocarbon pyrolysis, Combust. Flame 243 (2022) 111942, https://doi.org/10.1016/j.combustflame.2021.111942.
[130] H. Sabbah, M. Commodo, F. Picca, G. De Falco, P. Minutolo, A. D'Anna, C. Joblin, Molecular content of nascent soot: family characterization using two-step laser desorption laser ionization mass spectrometry, Proc. Combust. Inst. 38 (2021) 1241–1248, https://doi.org/10.1016/j.proci.2020.09.022.
[131] A. Nobili, L. Pratali Maffei, A. Baggioli, M. Pelucchi, A. Cuoci, C. Cavallotti, T. Faravelli, On the radical behavior of large polycyclic aromatic hydrocarbons in soot formation and oxidation, Combust. Flame 235 (2022) 111692, https://doi.org/10.1016/j.combustflame.2021.111692.
[132] Y. Wang, S.H. Chung, Soot formation in laminar counterflow flames, Prog. Energy Combust. Sci. 74 (2019) 152–238, https://doi.org/10.1016/j.pecs.2019.05.003.
[133] D. Wang, J. Yao, W. Dong, Z. Rui, W. Pan, H. Chu, Numerical investigation of soot formation in methane/n-heptane laminar diffusion flame doped with hydrogen at elevated pressure, Int. J. Hydrogen Energy 79 (2024) 1237–1249, https://doi.org/10.1016/j.ijhydene.2024.07.082.
[134] M.R. Kholghy, A. Veshkini, M.J. Thomson, The core–shell internal nanostructure of soot – a criterion to model soot maturity, Carbon 100 (2016) 508–536, https://doi.org/10.1016/j.carbon.2016.01.022.
[135] H.A. Michelsen, Effects of maturity and temperature on soot density and specific heat, Proc. Combust. Inst. 38 (2021) 1197–1205, https://doi.org/10.1016/j.proci.2020.06.383.
[136] M.A. Pimenta, G. Dresselhaus, M.S. Dresselhaus, L.G. Cançado, A. Jorio, R. Saito, Studying disorder in graphite-based systems by Raman spectroscopy, Phys. Chem. Chem. Phys. 9 (2007) 1276–1290, https://doi.org/10.1039/B613962K.
[137] S. Dasappa, J. Camacho, Evolution in size and structural order for incipient soot formed at flame temperatures greater than 2100 K, Fuel 291 (2021) 120196, https://doi.org/10.1016/j.fuel.2021.120196.
[138] A. Cuesta, P. Dhamelincourt, J. Laureyns, A. Martínez-Alonso, J.M.D. Tascón, Raman microprobe studies on carbon materials, Carbon 32 (1994) 1523–1532, https://doi.org/10.1016/0008-6223(94)90148-1.
[139] M. Commodo, G. Serra, S. Bocchicchio, P. Minutolo, M. Tommasini, A. D'Anna, Monitoring flame soot maturity by variable temperature Raman spectroscopy, Fuel 321 (2022) 124006, https://doi.org/10.1016/j.fuel.2022.124006.
[140] Z.-M. Wang, X. Zhang, J.-M. Lei, K.-R. Jin, Du Wang, Z.-Y. Tian, Revisit the PAH and soot formation in high-temperature pyrolysis of methane, J. Anal. Appl. Pyrolysis 182 (2024) 106668, https://doi.org/10.1016/j.jaap.2024.106668.
[141] Y. Wang, M. Gu, J. Wu, L. Cao, Y. Lin, X. Huang, Formation of soot particles in methane and ethylene combustion: a reactive molecular dynamics study, Int. J. Hydrogen Energy 46 (2021) 36557–36568, https://doi.org/10.1016/j.ijhydene.2021.08.125.
[142] H.A. Michelsen, Probing soot formation, chemical and physical evolution, and oxidation: a review of in situ diagnostic techniques and needs, Proc. Combust. Inst. 36 (2017) 717–735, https://doi.org/10.1016/j.proci.2016.08.027.
[143] E. Busillo, A. Nobili, F. Serse, M.P. Bracciale, P. De Filippis, M. Pelucchi, B. de Caprariis, Turquoise hydrogen and carbon materials production from thermal methane cracking: an experimental and kinetic modelling study with focus on carbon product morphology, Carbon 225 (2024) 119102, https://doi.org/10.1016/j.carbon.2024.119102.
[144] Y. Araki, Y. Matsukawa, Y. Saito, Y. Matsushita, H. Aoki, K. Era, T. Aoki, Effects of carrier gas on the properties of soot produced by ethylene pyrolysis, Fuel Process. Technol. 213 (2021) 106673, https://doi.org/10.1016/j.fuproc.2020.106673.